Model-independent features of gravitational waves from bubble collisions

Ariel Mégevand[*] and Federico Agustín Membiela[†]

IFIMAR (CONICET-UNMdP) Departamento de Física, Facultad de Ciencias Exactas y Naturales, UNMdP, Deán Funes 3350, (7600) Mar del Plata, Argentina

(Received 24 August 2021; revised 8 November 2021; accepted 24 November 2021; published 14 December 2021)

We study the gravitational radiation produced by the collisions of bubble walls or thin fluid shells in cosmological phase transitions. Using the so-called envelope approximation, we obtain analytically the asymptotic behavior of the gravitational wave spectrum at low and high frequencies for any phase transition model. The complete spectrum can thus be approximated by a simple interpolation between these asymptotes. We verify this approximation with specific examples. We use these results to discuss the dependence of the spectrum on the time and size scales of the source.

DOI: 10.1103/PhysRevD.104.123532

I. INTRODUCTION

In a phase transition of the Universe, the disturbance produced in the hot plasma is a source of interesting phenomena such as baryogenesis [1,2] or the formation of gravitational waves (GWs) [3]. In particular, a phase transition at the TeV scale gives naturally a GW spectrum that may be observable by the space-based interferometer LISA [4]. This fact has motivated the investigation of GW production in the electroweak phase transition, which may be strong enough in several extensions of the Standard Model [5–39]. Gravitational waves generated in other phase transitions have also been studied, as well as their detectability prospects [40–59]. In general, a cosmological phase transition can be modeled with a scalar order-parameter field $\phi(\mathbf{x}, t)$ which couples to a plasma composed of several species of relativistic particles. In the electroweak phase transition, this classical field represents the expectation value of the Higgs field. The value $\phi = 0$ corresponds to the symmetric, metastable phase, while a nonvanishing value corresponds to the stable, broken-symmetry phase.

In the case of a first-order phase transition, bubbles of the stable phase nucleate and expand into the supercooled metastable phase. A bubble is essentially a configuration in which the scalar field takes the stable-phase value in a certain region and vanishes outside. The expansion of bubbles is driven by the pressure difference between the two phases. In most cases the bubble walls reach a terminal velocity due to the friction with the plasma [60–75] and to hydrodynamic obstruction [76–86]. However, there are scenarios in which the wall undergoes a continuous acceleration or runaway behavior [87–89], especially when there is significant supercooling (see, e.g., [90–95]). In any case, the variation of temperature due to the adiabatic cooling or to reheating generally causes variations of the nucleation rate $\Gamma(t)$ and the wall velocity $v(t)$ as functions of time t (see, e.g., [96]).

A few different processes can produce GWs in a phase transition. The bubble collision mechanism is directly related to the propagation of the bubble walls [97]. On the other hand, the walls cause bulk fluid motions which may lead to gravitational radiation via turbulence [98–106] or sound waves [107–113], (see [114] for a review of these mechanisms). If the wall reaches a terminal velocity, most of the energy released in the transition will go to reheating and bulk fluid motions (see, e.g., [84,115]). In such scenarios the GW signal is dominated by the fluid mechanisms. On the other hand, in cases of continuous wall acceleration, an important fraction of the energy accumulates in the bubble walls (see, e.g., [84,86]) and the bubble collisions become important.

The envelope approximation for the bubble collision mechanism consists in modeling the bubble walls as infinitely thin spherical surfaces and considering only the uncollided parts of them as sources of GWs. The original calculation [116] was based on a simulation in which bubbles were nucleated at arbitrary points in space and with a distribution in time corresponding to a nucleation rate $\Gamma(t) \propto e^{\beta t}$, and their radii grew with a constant velocity v. This numerical computation was repeated in Refs. [117,118] with technical improvements such as considering more bubbles in the simulation. The resulting GW power spectrum has the form of a broken power law in frequency. Specifically, the spectrum rises as a power ω^a for low frequencies and falls as ω^{-b} for high frequencies, where a is close to 3 and b is close to 1. The peak frequency is of the order of the timescale β^{-1}. Lattice simulations for the evolution of the scalar field have also been used to

[*]megevand@mdp.edu.ar
[†]membiela@mdp.edu.ar

compute the GW spectrum from bubble collisions [118–121]. The precise value of the peak of the spectrum is found to be slightly shifted to lower frequencies with respect to the envelope approximation, and the exponent of the high-frequency power law varies from $b \simeq 1.5$ to $b \simeq 2.3$, depending on the wall width.

The envelope approximation has also been used to compute the gravitational radiation from bulk fluid motions, assuming that the fluid is concentrated in thin shells next to the walls [98,117]. In Ref. [118], such a computation was compared with a lattice simulation of the coupled system of scalar field and fluid. It was shown that, for GWs generated by the fluid during bubble collisions, the form of the spectrum is different for thick walls.[1] A more recent semianalytic calculation [122] for an exponentially growing nucleation rate and a constant wall velocity confirmed the broken power law, with $a = 3$ and $b = 1$. In this approach, only two integrals must be computed numerically, thus allowing us to reach a wider frequency range. A modification of the envelope approximation, the so-called bulk flow model, consists in considering thin fluid shells which persist after the walls collide. This model was investigated either with semianalytical calculations [123] and by simulating the formation and expansion of the thin fluid shells [124]. Recently, we discussed a more general semianalytic approach [125], which can be applied to the envelope or bulk-flow approximations, as well as to more general wall kinematics.

The relative simplicity of the envelope approximation is useful to study the dependence of the GW spectrum on the phase transition model. In the simulations of Ref. [118], a simultaneous nucleation as well as an exponentially growing nucleation rate were considered. In Ref. [126], the semianalytical method of [122] was applied to a nucleation model of the form $e^{\beta t-\gamma^2 t^2}$. In this case, the exponential and simultaneous nucleations are obtained in the limits of very low and very high γ, respectively. On the other hand, in the lattice simulations of Ref. [120], a constant nucleation rate was considered as well as the exponential and simultaneous cases. The different spectra obtained in these works are qualitatively similar, suggesting that the power laws at low and high frequencies do not depend on the nucleation rate. This also seems to indicate that the GW signal does not have a strong dependence on the distribution of bubble sizes, which is quite different for different nucleation rates.

It is worth mentioning that, for such a comparison between nucleation rates, the energy of the gravitational radiation is usually divided by the released vacuum energy, and the frequency ω is divided by some characteristic parameter ω_* which has the same meaning in the different scenarios. For instance, using the average final bubble separation d_b as a unit of frequency, $\omega_* = d_b^{-1}$ (see, e.g., [120]), the models under comparison have the same value of d_b. The parameter β of the exponential rate can also be used as a unit. Although this quantity is rather artificial for other models, it can be defined, e.g., by inverting the relation which holds for the exponential case, $d_b = (8\pi)^{1/3} v/\beta$ (this was used, e.g., in Ref. [114] to put the results of Ref. [109] in terms of β). For comparing only the shape of the spectrum, the peak frequency ω_p can be used [126]. The precise choice of ω_* in terms of some length or time associated to the phase transition kinematics will determine the relative position of the peak between different models.

In the present paper we use the envelope approximation to investigate the dependence of the GW spectrum on specific features of the phase transition, such as the nucleation rate and the wall velocity, and, more generally, on length and timescales of the source. The bubble collision mechanism is particularly suitable for that aim since it is the one that links more directly the kinematics of bubble nucleation and expansion to the GW spectrum. We also discuss a technique for finding the asymptotic behavior of the spectrum at high frequency. We obtain analytically the power laws ω^3 and ω^{-1} for the envelope approximation independently of $\Gamma(t)$ and $v(t)$. For the case of a constant wall velocity, we obtain analytically the dependence on the parameter v.

The plan of the paper is the following. In the next section we review the development of a first-order phase transition and we discuss the general definition of a characteristic timescale for general forms of $\Gamma(t)$ and $v(t)$. In Sec. III we discuss the definition of a dimensionless GW spectrum which is suitable for model comparison and we write down the expressions we shall use for the envelope approximation. In Sec. IV we investigate the form of the spectrum at low and high frequencies. In Sec. V we consider several specific cases, corresponding to a constant wall velocity and different nucleation rates (namely, an exponential, a delta function, a Gaussian, and a constant rate). In Sec. VI we use the results to discuss the dependence of the GW spectrum on the characteristics of the phase transition. We conclude with a discussion on the bubble collision mechanism in Sec. VII. More details on the calculations and on the numerical results, as well as analytic formulas and comparisons with previous approaches are given in the Appendices.

II. GENERAL PARAMETRIZATION OF BUBBLE KINEMATICS

In the envelope approximation, one considers bubble walls which are spherical surfaces (as bubbles overlap, the walls are assumed to disappear in the overlapping regions). In this picture, there is a homogeneous wall velocity $v(t)$. Thus, for a bubble nucleated at a certain time t_N, the radius at time t is given by

[1]Moreover, after bubble collisions, the acoustic and turbulent behaviors of the fluid cannot be modeled by the envelope approximation [111].

$$R(t_N,t)=\int_{t_N}^{t} v(t'')dt'', \tag{1}$$

where we have ignored for simplicity the scale factor (which is a good approximation if the transition is short enough), and we have assumed that the initial bubble size can be neglected (which is often the case). Assuming as well a homogeneous nucleation rate $\Gamma(t)$ per unit time per unit volume, and taking into account bubble overlapping, the average fraction of volume remaining in the high-temperature phase at time t is given by $f_+(t)=e^{-I(t)}$, with [127–129]

$$I(t)=\int_{-\infty}^{t} dt''\Gamma(t'')\frac{4\pi}{3}R(t'',t)^3. \tag{2}$$

The nucleation rate actually vanishes for $t<t_c$, where t_c is the time corresponding to the critical temperature, so the lower limit of integration in Eq. (2) can be replaced by t_c. However, doing so is somewhat misleading, since in most cases $\Gamma(t)$ is actually negligible still at later times $t>t_c$, so the quantity $I(t)$ does not really depend on the value of t_c.

The general form of the nucleation rate as a function of the temperature T is

$$\Gamma=A\exp[-S(T)], \tag{3}$$

where S is the instanton action. For a vacuum transition [130,131], S is a constant and the factor A is of order M^4, where M is the energy scale of the model. For a thermal transition, we have $A\sim T^4$. In this case [132,133], S has a strong dependence on the temperature, the dynamics of nucleation is dominated by the exponential, and the specific form of the prefactor is not too relevant. The adiabatic cooling of the Universe causes in principle a rapid growth of Γ with time. However, depending on the global dynamics of the phase transition, Γ may begin to decrease at a certain point, as quickly as it previously grew. Two possible scenarios for such a decrease are the system getting stuck in the false vacuum (in the case of a very strong phase transition), or a reheating of the plasma, which occurs when the phase transition is mediated by slow deflagration bubbles (see Refs. [90,134] for recent discussions).

In practice, bubble nucleation becomes noticeable at a certain time t_*, after Γ becomes of order H^4, where H is the Hubble rate. Then, in general, bubbles fill all the space in a short time $t_b\ll H^{-1}$. The kinematics of bubble nucleation and growth may involve different characteristic times. For instance, $\Gamma(t)$ may turn off in a relatively short time due to reheating, after which bubble expansion may continue for a longer time [134]. We shall denote by t_Γ the time associated to bubble nucleation. Without loss of generality, we can always define a dimensionless function $f(\tau)$ such that we can write

$$\Gamma(t)=\Gamma_* f\left(\frac{t-t_*}{t_\Gamma}\right), \quad \text{with} \quad f(0)=1, \tag{4}$$

so that $\Gamma_*=\Gamma(t_*)$ for a certain reference time t_*. Since in general $\Gamma(t)$ has a very rapid variation, the prefactor Γ_* is rather meaningless unless the time t_* is inside, or very close to, the time interval in which the phase transition effectively occurs (i.e., where most bubbles nucleate and the fraction of volume f_+ has a significant variation). The number density of bubbles,

$$n_b=\int_{-\infty}^{+\infty}\Gamma(t)f_+(t)dt, \tag{5}$$

defines a characteristic length scale $d_b\equiv n_b^{-1/3}$, which is an estimate of the average distance between nucleation centers. For cases in which the nucleation rate reaches a maximum at a time t_m within the relevant time interval (we consider specific examples below), a convenient choice for the parameter t_* is $t_*=t_m$. If Γ does not have a maximum but grows indefinitely, the time t_* can be associated, e.g., to the maximum of the effective nucleation rate $\Gamma(t)e^{-I(t)}$. In any case, by definition of t_Γ we have $n_b\sim\Gamma_* t_\Gamma$, and we can write[2]

$$\Gamma(t)=\frac{1}{t_\Gamma d_b^3}g\left(\frac{t-t_*}{t_\Gamma}\right), \quad \text{with} \quad g(0)\sim 1. \tag{6}$$

The relation between the time parameter t_Γ and the distance parameter d_b depends on the global dynamics of the phase transition. In particular, these parameters may not be directly related through the velocity of bubble expansion. As already mentioned, the duration of the phase transition t_b may differ from the nucleation time t_Γ. The time t_b is more directly related to the average bubble size d_b through the average bubble wall velocity. We thus define a velocity parameter $v_b=d_b/t_b$. If the two timescales are different, it is convenient to define the parameter $\alpha=t_b/t_\Gamma$ and the function $\tilde{\Gamma}(\tau)=\alpha g(\alpha\tau)$. Thus, we may write Eq. (6) in terms of t_b and v_b,

$$\Gamma(t)=\frac{1}{v_b^3 t_b^4}\tilde{\Gamma}\left(\frac{t-t_*}{t_b}\right), \quad \text{with} \quad \tilde{\Gamma}(0)\sim t_b/t_\Gamma. \tag{7}$$

In the simplest cases, we have a single timescale, $t_b\sim t_\Gamma$, so $\tilde{\Gamma}(0)\sim 1$. The different parametrizations we have discussed are useful for different purposes, and in the rest of this paper we shall use the form (7).

[2]We could actually define the parameters t_* and t_Γ such that we have exactly $\Gamma_* t_\Gamma=n_b$, so that we would just have $g(\tau)=f(\tau)$ in Eq. (6). However, we want to have the freedom to choose the parameters conveniently for the simplicity of the expression for $\Gamma(t)$. Therefore, we relax the condition $f(0)=1$ to $g(0)\sim 1$.

Let us consider a few simple examples which span the different possibilities for the relation between t_b and t_Γ.

A. Constant nucleation rate

As mentioned above, for a vacuum phase transition the nucleation rate is a constant. In a physical particle-physics model, this scenario could arise in the case of extreme supercooling, i.e., if the system is stuck in the metastable phase even when the temperature is much smaller than the critical temperature. In such a case the energy density is dominated by vacuum energy and the Universe undergoes inflation (see, e.g., [90]), unless the phase transition occurs in a hidden sector, such that the visible sector dominates the energy density (see, e.g., [54]). In the latter case, the nucleation of bubbles will effectively occur when the condition $\Gamma \sim H^4$ is satisfied, where the evolution of the Hubble rate $H(t)$ is determined by the temperature of the visible sector. Hence, the dynamics of such a phase transition departs from the more common scenario in which the variation of H is neglected.

For a thermal phase transition, a constant nucleation rate will hardly be a good approximation since the instanton action $S(T)$ is very sensitive to temperature variations. A scenario in which the temperature remains approximately constant arises when bubbles expand as slow deflagrations, where the temperature outside the bubbles is heated up by shock fronts which carry away the released latent heat (see, e.g., [134]). In this case there is a reheated stage in which the temperature is approximately constant and homogeneous. However, this temperature is higher than in the previous pre-reheating stage, so this constant rate is vanishingly small in comparison. Hence, the bubble nucleation effectively occurs in a small time interval at the beginning of bubble expansion, and a better approximation for $\Gamma(t)$ is a Gaussian or a delta function.

In spite of this, the approximation of a constant nucleation rate is often used in time-consuming computations such as lattice simulations, so we shall discuss it here. In the parametrization (7), this case corresponds to the limit of $t_\Gamma \gg t_b$, while the opposite case $t_\Gamma \ll t_b$ corresponds to a delta-function rate (considered below). This model requires also assuming that the bubble nucleation turns on at a certain time t_0. Thus, we have $\Gamma = \Gamma_0 \Theta(t - t_0)$. For a constant velocity v, a trivial calculation gives $I(t) = \frac{\pi}{3} v^3 \Gamma_0 (t - t_0)^4$, so the fraction of volume in the old phase is given by $f_+ = e^{-[(t-t_0)/t_b]^4}$, with $t_b = (\frac{\pi}{3} v^3 \Gamma_0)^{-1/4}$. The parameter t_b is associated to the duration of the phase transition, and we may use a parametrization of the form (7),

$$\Gamma(t) = \frac{1}{v^3 t_b^4} \frac{3}{\pi} \Theta\left(\frac{t - t_0}{t_b}\right), \tag{8}$$

with $t_* = t_0$ and $\tilde{\Gamma}(\tau) = \frac{3}{\pi} \Theta(\tau)$. The parameter d_b defined from the bubble number density is not exactly given by $v t_b$. A simple calculation gives $n_b = \int_{-\infty}^{+\infty} \Gamma(t) e^{-I(t)} dt = (3/\pi)\Gamma(5/4) v^{-3} t_b^{-3}$ (where the last Γ symbol represents the Euler gamma function). Therefore, we have $d_b \simeq 0.98 v t_b$ (i.e., the velocity parameter defined by $v_b = d_b/t_b$ does not coincide exactly with the velocity v).

B. Exponential nucleation rate

The exponential nucleation rate $\Gamma(t) = \Gamma_* e^{\beta(t-t_*)}$ is obtained by linearizing the instanton action $S(T(t))$ at the time t_*. For a constant velocity, this rate gives $I(t) = 8\pi v^3 \Gamma(t)/\beta^4$, and the fraction of volume varies from the asymptotic value $f_+ = 1$ for $t \to -\infty$ to $f_+ = 0$ for $t \to \infty$. Nevertheless, most of the variation occurs in a time interval of order β^{-1}. If t_* is not close enough to this interval, then the parameter Γ_* will not give even the order of magnitude of $\Gamma(t)$ at the relevant times. Whatever the values of the original parameters t_* and Γ_*, we may write $\Gamma(t) = \Gamma'_* e^{\beta(t-t'_*)}$, where the new and old parameters are related by $\Gamma'_* = \Gamma_* e^{\beta(t'_*-t_*)}$. A convenient choice for t'_* is the time t_e for which $I(t_e) = 1$, i.e., when f_+ has decreased to e^{-1}. Indeed, at $t = t_e$ the average nucleation rate $\Gamma(t) f_+(t)$, as well as the total uncollided wall area $\langle S_{\rm tot}(t) \rangle$, take their maximum [135]. By definition of t_e we have $I(t) = e^{\beta(t-t_e)}$, so we may write

$$\Gamma(t) = \frac{\beta^4}{8\pi v^3} e^{\beta(t-t_e)}. \tag{9}$$

Taking into account the well known relation $d_b = (8\pi)^{1/3} v/\beta$, we have $\Gamma(t) = \beta d_b^{-3} e^{\beta(t-t_e)}$, which is of the form (6) with $t_\Gamma = \beta^{-1}$. If we define $t_b = t_\Gamma = \beta^{-1}$, Eq. (9) is also of the form (7) and we have $\tilde{\Gamma}(\tau) = e^\tau/8\pi$. Here, we have $\tilde{\Gamma}(0) = 1/8\pi \neq t_b/t_\Gamma$, since a different time parameter $t'_b > \beta^{-1}$ would actually be more representative of the duration of the phase transition (see, e.g., [135]). Nevertheless, we shall use the form (9) since β is the standard parameter.

C. Gaussian nucleation rate

As already mentioned, there are at least two different scenarios in which the nucleation rate may reach a maximum and turn off during the phase transition:

(A) Strong supercooling: $S(T)$ has a minimum.
(B) Reheating: $T(t)$ has a minimum.

Case A occurs when a barrier between the minima of the effective potential persists at low temperatures [90]. In such a case, the nucleation rate initially grows as the temperature descends from the critical temperature T_c and the minima become nondegenerate. However, at low enough temperature the barrier between phases cannot be surpassed and the nucleation rate begins to decrease with decreasing temperature. Correspondingly, the instanton action $S(T)$ has a minimum at a certain temperature T_m. Since T

decreases as a function of time, this minimum will be reached at a certain time t_m (unless the phase transition is completed before that time). Expanding $S(t)$ around its minimum, we obtain a Gaussian approximation for the nucleation rate,

$$\Gamma(t) = \Gamma_m \exp[-\gamma^2 (t - t_m)^2]. \tag{10}$$

Case B occurs when a phase transition is mediated by slow deflagrations [134]. In the general scenario there is little supercooling, since the barrier between minima disappears at a temperature which is close to the critical one, and in this range $S(T)$ is a monotonous function. However, for walls which propagate as deflagrations, the plasma outside the bubbles is reheated during the phase transition. As a result, the temperature initially decreases due to the adiabatic expansion of the Universe, but at some point it begins to increase due to reheating. As a consequence, the temperature $T(t)$ has a minimum at a certain time t_m, and so does the function $S(T(t))$, so the nucleation rate can be approximated again by Eq. (10).

In case B, the maximum of the nucleation rate is always reached during the phase transition, since the very existence of a minimum of $T(t)$ is due to the reheating during bubble expansion. In contrast, in case A the function $\Gamma(T)$ has a maximum at a temperature T_m which may not be reached during the phase transition. This will happen if Γ_m is very large compared to H^4. In such a case, the phase transition will complete at an earlier time t_* such that $\Gamma(t_*) \sim H(t_*)^4$. If this is the case, it is not a good approximation to expand $S(T)$ at T_m. Expanding at a higher temperature T_* will give a linear term, while the quadratic term is a second order correction. Hence an exponential nucleation rate will not be a bad approximation. This case was considered in Ref. [126], and we discuss it in some detail in Appendix B. On the other hand, in cases for which the maximum of $\Gamma(t)$ is reached during the phase transition,[3] we have a "true Gaussian rate", i.e., it cannot be approximated by an exponential rate.

The nucleation rate (10) is of the form (4), with $t_* = t_m$, $\Gamma_* = \Gamma_m$, and $t_\Gamma = \gamma^{-1}$. An interesting difference from the previous cases is that, since the nucleation rate turns off, there is a bound on the number of nucleated bubbles, namely,

$$n_{\max} = \int_{-\infty}^{+\infty} \Gamma(t) dt = \sqrt{\pi} \Gamma_m / \gamma. \tag{11}$$

The actual number density (5) contains a factor $f_+(t)$, which implies $n_b < n_{\max}$. This bound defines a minimal bubble separation, $d_{\min} = n_{\max}^{-1/3}$. Unless the phase transition finishes before the maximum of the Gaussian is reached, the value $n_{\max}$ will be a good approximation for n_b, and we have $d_b \simeq d_{\min}$ (see Appendix B for more details). In terms of this parameter, Eq. (10) becomes

$$\Gamma(t) = (\gamma/\sqrt{\pi} d_{\min}^3) \exp[-\gamma^2 (t - t_m)^2], \tag{12}$$

which is of the form (6) with $g(\tau) = e^{-\tau^2}/\sqrt{\pi}$. The time $t_b = d_b/v_b$ may be different from the nucleation time t_Γ (in particular, the phase transition may go on after the nucleation rate turns off). In order to write Eq. (12) in the form (7), we shall use the analytic parameter $t_{\min} = d_{\min}/v_b$ instead of t_b which must be obtained numerically. We have

$$\Gamma(t) = \frac{1}{v_b^3 t_{\min}^4} \tilde{\Gamma}\left(\frac{t - t_m}{t_{\min}}\right), \tag{13}$$

where $\tilde{\Gamma}(\tau) = \gamma t_{\min} g(\gamma t_{\min} \tau)$. Since we have two different timescales, the dimensionless nucleation rate depends on the parameter $\alpha \equiv \gamma t_{\min} = t_{\min}/t_\Gamma$.

D. Delta-function nucleation rate

If the time during which nucleation occurs is much shorter than the total duration of the phase transition, the nucleation rate can be approximated by a delta function $\Gamma(t) = n_b \delta(t - t_*)$, where n_b is the number density of bubbles. This can be regarded as a limit of the Gaussian rate, and is a good approximation for some models of type B (in the classification of the previous subsection). In particular, when a sudden reheating of the plasma causes the nucleation rate to quickly turn off [134]. Since the nucleation in this case is simultaneous, the fundamental parameter is the distance scale $d_b \equiv n_b^{-1/3}$. Using the well-known scaling property of the delta distribution, we may write

$$\Gamma(t) = \frac{1}{t_b d_b^3} \delta\left(\frac{t - t_*}{t_b}\right) \tag{14}$$

for any parameter t_b. The convenient time parameter here is the typical time of bubble growth. Given a characteristic (average) velocity v_b, we have $t_b = d_b/v_b$. Hence, Eq. (14) is of the form (7) with $\tilde{\Gamma}(\tau) = \delta(\tau)$. This can also be obtained as the limit for $\alpha \to \infty$ of the Gaussian case $\tilde{\Gamma}(\tau) = \alpha g(\alpha \tau)$.

III. GRAVITATIONAL WAVES

The gravitational wave power spectrum is often represented by the quantity

$$\Omega_{\rm GW} = \frac{1}{\rho_{\rm tot}} \frac{d\rho_{\rm GW}}{d \ln \omega}, \tag{15}$$

i.e., the energy density in gravitational radiation per logarithmic frequency, divided by the total energy density

[3] It is worth commenting that, in case A, if Γ_m is too low in comparison with the expansion parameter H^4, the phase transition will never complete (see [90] for details).

of the Universe, $\rho_{\rm tot}$. Before proceeding to the calculation of this quantity, we shall discuss the definition of a dimensionless quantity which is useful for expressing general results and for model comparison.

A. Dimensionless GW spectrum

The quantity (15) is sometimes written in the form (see, e.g., [117,122])

$$\Omega_{\rm GW} = \kappa^2 \left(\frac{H}{\beta}\right)^2 \left(\frac{\alpha_T}{\alpha_T + 1}\right)^2 \Delta(\omega/\beta), \tag{16}$$

where β is the parameter of the exponential nucleation rate, α_T is the ratio of the energy released at the phase transition to the radiation energy, $\alpha_T = \rho_{\rm vac}/\rho_{\rm rad}$, κ is an efficiency factor [98] quantifying the fraction of the released energy which goes into the source of GWs, and the dimensionless function Δ is defined as

$$\Delta(\omega/\beta) \equiv \frac{3\beta^2}{8\pi G(\kappa\rho_{\rm vac})^2} \frac{d\rho_{\rm GW}}{d\ln\omega}(\omega). \tag{17}$$

In these expressions, the quantities κ^2, $\rho_{\rm vac}^2$, and β^2 are introduced just by multiplying and dividing them in Eq. (15). The other quantities are introduced by using the relation $H^2 = 8\pi G\rho_{\rm tot}/3$, assuming that the total energy density can be decomposed into vacuum and radiation energy densities, $\rho_{\rm tot} = \rho_{\rm vac} + \rho_{\rm rad}$, and assuming that the vacuum energy density coincides with the latent heat released at the phase transition. These approximations can be improved (see [136,137] for recent discussions), but are useful to focus on the calculation of the dimensionless quantity Δ for a simplified phase transition kinematics and then applying Eq. (16) to specific realistic models (see, e.g., [93,114]).

Under suitable approximations, the quantity $(\kappa\rho_{\rm vac})^2$ is a constant which will appear explicitly in the expression for $d\rho_{\rm GW}/d\ln\omega$ and cancel out in Eq. (17), as well as the numerical constants. On the other hand, using the parameter β makes sense only for the exponential nucleation rate, since for other cases the expression for $d\rho_{\rm GW}/d\ln\omega$ will depend on a different quantity. Nevertheless, we may generalize the definition of Δ in terms of a more general reference frequency ω_*,

$$\Delta(\omega/\omega_*) \equiv \frac{3\omega_*^2}{8\pi G(\kappa\rho_{\rm vac})^2} \frac{d\rho_{\rm GW}}{d\ln\omega}(\omega). \tag{18}$$

For a given mechanism of GW generation, the parameter ω_* can be conveniently associated to a relevant time or length scale.[4] Thus, for bubble collisions, it is convenient to use the frequency $\omega_b = t_b^{-1}$ associated to the time parameter which appears explicitly in the parametrization (7) and depends on the specific phase transition model. However, for comparing two different models a single frequency unit must be used. The relation between the dimensionless spectrum for two different reference frequencies is $\Delta_2(\omega/\omega_2) = (\omega_2/\omega_1)^2\Delta_1((\omega_2/\omega_1)(\omega/\omega_2))$.

B. GWs from bubble walls

We shall use the approach of Ref. [125], which we summarize very briefly. For a large volume V, the GW power spectrum is written in the form

$$\frac{d\rho_{\rm GW}}{d\ln\omega} = \frac{4G\omega^3}{\pi} \int_{-\infty}^{\infty} dt \int_t^{\infty} dt' \cos[\omega(t-t')]\Pi(t,t',\omega), \tag{19}$$

where

$$\Pi(t,t',\omega) \equiv \frac{1}{V}\Lambda_{ij,kl}(\hat{n})\langle \tilde{T}_{ij}(t,\omega\hat{n})\tilde{T}_{kl}(t',\omega\hat{n})^*\rangle, \tag{20}$$

$\Lambda_{ij,kl}$ is the transverse-traceless projection tensor for the direction of observation $\hat{n}$, $\tilde{T}_{ij}$ is the spatial Fourier transform of the stress-energy tensor T_{ij} of the source, and $\langle\rangle$ indicates ensemble average. If T_{ij} is decomposed as a sum over bubbles, Π naturally separates as $\Pi = \Pi^{(s)} + \Pi^{(d)}$, where $\Pi^{(s)}$ contains correlations between different points on a single bubble and $\Pi^{(d)}$ contains correlations between two different bubbles (such a separation also arises in the treatment of Ref. [122]). For gravitational waves from bubble walls, T_{ij} is approximated by a surface delta function which eliminates some of the spatial integrals in the Fourier transforms $\tilde{T}_{ij}$, $\tilde{T}_{kl}$. In the case of the envelope approximation we have, for each bubble,

$$T_{ij} = \sigma\delta(r-R)\hat{r}_i\hat{r}_j 1_S(\hat{r}), \tag{21}$$

where σ is the surface energy density, r is the distance from the bubble center, R is the bubble radius, $R\hat{r}$ is the position of a point on the bubble surface, and 1_S is the indicator function for the uncollided wall. To take into account the energy which accumulates in the wall, the usual replacement $\sigma = (\kappa\rho_{\rm vac}/3)R$ is made, where the efficiency factor κ accounts for the fraction of energy which goes either to the wall (in a vacuum phase transition we have $\kappa = 1$) or to bulk fluid motions (which are assumed to occur in thin shells next to the walls) (see, e.g., [6,16,84,86,92,115,138–141] for the calculation of this factor). Finally, the sum over bubbles and the statistical average are related to the nucleation rate $\Gamma(t)$, and several of the remaining angular integrals can be performed analytically.

The result depends on the probability that two points at angular positions $\hat{r}$, $\hat{r}'$ on the bubble surfaces at times t and

[4]It is worth noticing that this characteristic frequency determines the peak of the spectrum at the time of GW generation. The frequency, as well as the energy density, are subject to redshifting.

t' are both uncollided. This probability was studied in Ref. [135]. It is proportional to $e^{-I(t)}e^{-I(t')}e^{I_\cap}$, where the last factor takes into account the fact that the probabilities for the two points are not independent.[5] We have

$$I_\cap(t,t',s)=\int_{-\infty}^{t}dt''\Gamma(t'')V_\cap(t'',t,t',s), \tag{22}$$

where s is the distance between the points and

$$V_\cap=\frac{\pi}{12}(r+r'-s)^2\left[s+2(r+r')-\frac{3(r-r')^2}{s}\right]\times\Theta(r+r'-s). \tag{23}$$

Here, Θ is the Heaviside step function, and we have used the notation $r=R(t'',t)$, $r'=R(t'',t')$ (for more details and interpretation, see [135] or [125]). The final expressions from Ref. [125] (see [123] for similar expressions) are

$$\frac{\Pi^{(s)}(t,t',\omega)}{(\kappa\rho_{\rm vac}/3)^2}=\frac{\pi^2}{4}\int_{-\infty}^{t}dt_N\Gamma(t_N)\int_{R_-}^{R_+}\frac{ds}{s^3}\sum_{i=0}^{2}P_i(R_+,R_-,s)\times\frac{j_i(\omega s)}{(\omega s)^i}e^{-I_{\rm tot}(t,t',s)}, \tag{24}$$

$$\frac{\Pi^{(d)}(t,t',\omega)}{(\kappa\rho_{\rm vac}/3)^2}=\frac{\pi^3}{4}\int_{-\infty}^{t}dt_N\Gamma(t_N)\int_{-\infty}^{t'}dt'_N\Gamma(t'_N)\times\int_{R_-}^{R_+-|R(t_N,t'_N)|}\frac{ds}{s^4}e^{-I_{\rm tot}(t,t',s)}\frac{j_2(\omega s)}{(\omega s)^2}\times Q_+(s,R,R_-)Q_-(s,R',R_-), \tag{25}$$

where $I_{\rm tot}=I(t)+I(t')-I_\cap(t,t',s)$, the j_i are spherical Bessel functions,

$$j_0(x)=\frac{\sin x}{x},\qquad j_1(x)=\frac{\sin x-x\cos x}{x^2},\qquad j_2(x)=\frac{(3-x^2)\sin x-3x\cos x}{x^3}, \tag{26}$$

and the P_i and $Q_\pm$ are polynomials in R and R', which have simpler expressions in terms of the variables $R_+=R'+R$ and[6] $R_-=R(t,t')$,

$$P_0(R_+,R_-,s)=(s^2-R_-^2)^2(s^2-R_+^2)^2, \tag{27}$$

$$P_1(R_+,R_-,s)=2(s^2-R_-^2)(s^2-R_+^2)\times[3s^4+s^2(R_-^2+R_+^2)-5R_-^2R_+^2], \tag{28}$$

$$P_2(R_+,R_-,s)=3s^8+2s^6(R_-^2+R_+^2)+3s^4(R_-^4+4R_-^2R_+^2+R_+^4)-30s^2R_-^2R_+^2(R_-^2+R_+^2)+35R_-^4R_+^4 \tag{29}$$

and

$$Q_+(s,R,R_-)=(s^2-R_-^2)[(2R+R_-)^2-s^2]\times[s^2-R_-(2R+R_-)], \tag{30}$$

$$Q_-(s,R',R_-)=(s^2-R_-^2)[(2R'-R_-)^2-s^2]\times[s^2+R_-(2R'-R_-)]. \tag{31}$$

Now, we insert these results in the GW energy density (19) and then in the dimensionless spectrum (18). We obtain $\Delta=\Delta^{(s)}+\Delta^{(d)}$, with

$$\Delta^{(s)}=\frac{\omega^3\omega_*^2}{48}\int_{-\infty}^{\infty}dt_+\int_0^{\infty}dt_-\cos(\omega t_-)\int_{-\infty}^{t}dt_N\Gamma(t_N)\times\int_{R_-}^{R_+}\frac{ds}{s^3}e^{-I_{\rm tot}(t,t',s)}\sum_{i=0}^{2}\frac{j_i(\omega s)}{(\omega s)^i}P_i(R_+,R_-,s), \tag{32}$$

$$\Delta^{(d)}=\frac{\pi\omega^3\omega_*^2}{48}\int_{-\infty}^{\infty}dt_+\int_0^{\infty}dt_-\cos(\omega t_-)\times\int_{-\infty}^{t}dt_N\Gamma(t_N)\int_{-\infty}^{t'}dt'_N\Gamma(t'_N)\times\int_{R_-}^{R_+-|R(t_N,t'_N)|}\frac{ds}{s^4}e^{-I_{\rm tot}(t,t',s)}\frac{j_2(\omega s)}{(\omega s)^2}Q_+(s,R,R_-)\times Q_-(s,R',R_-). \tag{33}$$

where we have changed the variables t, t' to $t_\pm=t'\pm t$.

IV. ASYMPTOTIC BEHAVIOR

Before considering specific examples, we shall study the general behavior of the GW spectrum for low and high frequencies.

A. Low frequency

A general argument based on causality shows that for a transient stochastic source the low frequency tail of the GW spectrum $\Omega_{\rm GW}$ is proportional to ω^3 (see [142] and the more recent review [143]). It is worth remarking that this is the expected behavior in the far infrared (i.e., beyond causality), and is not necessarily the power law closer to the peak of the spectrum. As an example, for the bulk flow model with long-lasting fluid shells, the GW spectrum behaves as $\propto\omega^1$ below the peak frequency, and then

[5] If the points belong to the surfaces of two different bubbles, the probability includes also Heaviside functions which vanish if the bubbles are so close that one of the points has been captured by the other bubble.

[6] Notice that $R_-=\int_t^{t'}v_w(t'')dt''$ is given by $R'-R$ only for the single-bubble case (for the two-bubble case the latter difference depends on the nucleation times t_N,t'_N).

becomes $\propto \omega^3$ for smaller ω [123]. In the limit in which the fluid shells last forever, the low frequency limit is $\propto \omega^1$ since the bubbles keep expanding and, hence, producing GWs in the infrared [124]. This was shown analytically in Ref. [123], and below we use similar considerations for the envelope approximation. In this case, the source of GWs turns off as soon as the phase transition ends since the bubble walls disappear. As already mentioned, the power law ω^3 has been verified numerically for the bubble collision mechanism in the envelope approximation.

In Eqs. (32)–(33), the time variables $t_\pm$ have an effective range of order t_b around the time t_*, since the exponential $e^{-I_{\rm tot}}$, like $e^{-I(t)}$, becomes negligible at later times. As a consequence, the spatial variable s is bounded by $\sim v_b t_b$. Hence, for $\omega \ll t_b^{-1}$, the oscillating functions in the integrand can be expanded in powers of ω. The zeroth order corresponds to the replacements

$$\cos(\omega t_-) \to 1, \qquad j_0(\omega s) \to 1, \qquad \frac{j_1(\omega s)}{\omega s} \to \frac{1}{3}, \qquad \frac{j_2(\omega s)}{(\omega s)^2} \to \frac{1}{15}, \tag{34}$$

and the quantity Δ becomes, at low frequencies,

$$\Delta_{LF} = \Delta_{LF}^{(s)} + \Delta_{LF}^{(d)} = (B^{(s)} + B^{(d)})\omega^3, \tag{35}$$

where[7]

$$B^{(s)} = \frac{\omega_*^2}{48}\int_{-\infty}^{\infty} dt_+ \int_0^{\infty} dt_- \int_{-\infty}^{t} dt_N \Gamma(t_N) \times \int_{R_-}^{R_+} \frac{ds}{s^3}\left[P_0 + \frac{P_1}{3} + \frac{P_2}{15}\right] e^{-I_{\rm tot}}, \tag{36}$$

and

$$B^{(d)} = \frac{\pi\omega_*^2}{48}\int_{-\infty}^{\infty} dt_+ \int_0^{\infty} dt_- \int_{-\infty}^{t} dt_N \Gamma(t_N) \int_{-\infty}^{t'} dt'_N \Gamma(t'_N) \times \int_{R_-}^{R_+ - |R(t_N,t'_N)|} ds \frac{Q_+ Q_-}{15 s^4} e^{-I_{\rm tot}}. \tag{37}$$

B. High frequency

For $\omega \gg t_b^{-1}$, all the quantities appearing in Eqs. (32) and (33) have a slow variation in comparison with the oscillating functions $\cos(\omega t_-)$ and $j_i(\omega s)$. We change to variables $x = \omega s$ and $y = \omega t_-$ in order to eliminate the frequency from the latter, and then we define $\epsilon \equiv 1/\omega$ and expand the quantities in powers of ϵ. In the first place, we have

$$t = t_+/2 - \epsilon y/2, \qquad t' = t_+/2 + \epsilon y/2, \qquad s = x\epsilon. \tag{38}$$

For the bubble radius (1), we obtain

$$R = \bar{R} - \epsilon \bar{v} y/2 + \mathcal{O}(\epsilon^2), \qquad R' = \bar{R}' + \epsilon \bar{v} y/2 + \mathcal{O}(\epsilon^2), \tag{39}$$

where $\bar{R} \equiv R(t_N, \bar{t})$, $\bar{R}' \equiv R(t'_N, \bar{t})$, $\bar{v} \equiv v(\bar{t})$, and $\bar{t} = t_+/2$ ($\bar{R}$ and $\bar{R}'$ are equal for the single-bubble case). Hence, we have[8] $R_- = \epsilon \bar{v} y + \mathcal{O}(\epsilon^3)$, $R_+ = 2\bar{R} + \mathcal{O}(\epsilon^2)$. From Eq. (2) we obtain

$$I(t) + I(t') = 2I(\bar{t}) + O(\epsilon^2) \tag{40}$$

and, from Eqs. (22) and (23),

$$I_\cap(t, t', s) = I(\bar{t}) - \epsilon\pi \frac{x^2 + \bar{v}^2 y^2}{x} I_2(\bar{t}) + O(\epsilon^2), \tag{41}$$

where we have used the notation

$$I_n(t) = \int_{-\infty}^{t} dt'' \Gamma(t'') R(t'', t)^n \tag{42}$$

(the function I_3 is proportional to I). We thus have

$$e^{-I_{\rm tot}} = e^{-I(\bar{t})}\left[1 - \epsilon\pi I_2(\bar{t}) \frac{x^2 + \bar{v}^2 y^2}{x} + \mathcal{O}(\epsilon^2)\right]. \tag{43}$$

Let us consider first the single-bubble contribution,

$$\Delta^{(s)} = \frac{\epsilon^{-4}\omega_*^2}{24}\int_{-\infty}^{\infty} d\bar{t} \int_0^{\infty} dy \cos y \int_{-\infty}^{\bar{t} - \epsilon y/2} dt_N \Gamma(t_N) \times \int_{\bar{v} y + \mathcal{O}(\epsilon^2)}^{2\bar{R}/\epsilon + \mathcal{O}(\epsilon)} \frac{dx}{x^3} \sum_{i=0}^{2} \frac{j_i(x)}{x^i} P_i e^{-I(\bar{t})} \times \left[1 - \epsilon\pi I_2(\bar{t}) \frac{x^2 + \bar{v}^2 y^2}{x} + O(\epsilon^2)\right] \tag{44}$$

The first term inside the brackets gives a vanishing contribution upon integrating the variable x.[9] Therefore, the bracket gives a factor of ϵ. Besides, it is easy to see that the polynomials P_i, Eqs. (27)–(29), are of order ϵ^4,

$$P_i(R_+, \epsilon y, \epsilon x) = 16\epsilon^4 \bar{R}^4 p_i(x, \bar{v} y) \tag{45}$$

with

[7] We remark that the general definition of R_- is $R_- = R(t, t')$, and the expression $R_- = R' - R$ is valid only for the single-bubble case.

[8] For any smooth function $f(t)$, we have $f(t') - f(t) = f'(\bar{t})\epsilon y + \mathcal{O}(\epsilon^3)$ and $f(t) + f(t') = 2f(\bar{t}) + f''(\bar{t})\epsilon^2 y^2/4 + \mathcal{O}(\epsilon^4)$. We use these identities a couple of times below.

[9] Indeed, we have $\int_{R_-}^{R_+} \frac{ds}{s^3} \sum_{i=0}^{2} \frac{j_i(\omega s)}{(\omega s)^i} P_i = 0$ (to all order in ϵ), which is a consequence of the fact that $\int d\hat{r} \int d\hat{r}' e^{i\omega \hat{n}\cdot\mathbf{s}} \Lambda_{ijkl} \hat{r}_i \hat{r}_j \hat{r}'_k \hat{r}'_l = 0$. The reason is that the approximation $I_{\rm tot} = I(\bar{t})$ restores the spherical symmetry, since only the dependence of $I_\cap$ on the variable s carries the information on the correlation between different points on the walls.

$$p_0 = (x^2 - \bar{v}^2 y^2)^2, \qquad p_1 = -2(x^2 - \bar{v}^2 y^2)(x^2 - 5\bar{v}^2 y^2),$$
$$p_2 = 3x^4 - 30x^2\bar{v}^2 y^2 + 35\bar{v}^4 y^4. \tag{46}$$

Therefore, we have $\Delta^{(s)} \sim \epsilon = \omega^{-1}$. To this lowest order, we take the zeroth order in the limits of the integrals in Eq. (44). In this limit, the integration over the nucleation time only affects the factor $\bar{R}^4$, and gives a factor $I_4(\bar{t})$. Interchanging the order of the integrals with respect to x and y, we obtain

$$\Delta^{(s)} = -\frac{2\pi}{3}\omega_*^2\omega^{-1}\int_{-\infty}^{\infty} d\bar{t} e^{-I(\bar{t})} I_2(\bar{t}) I_4(\bar{t}) \times \int_0^{\infty} \frac{dx}{x^3} \sum_{i=0}^{2} \frac{j_i(x)}{x^i} \int_0^{x/\bar{v}} dy \cos y (x^2 + \bar{v}^2 y^2) p_i(x, \bar{v}y) + \mathcal{O}(\omega^{-2}). \tag{47}$$

The integrations on x and y can be done analytically, and we obtain

$$\Delta^{(s)}_{HF} = \omega^{-1}\frac{\pi\omega_*^2}{72}\int_{-\infty}^{\infty} d\bar{t} I_4(\bar{t}) I_2(\bar{t}) e^{-\frac{4\pi}{3}I_3(\bar{t})} A^{(s)}(\bar{v}) \tag{48}$$

(where the notation HF indicates the high frequency limit), with

$$A^{(s)}(\bar{v}) = 2\frac{3 - 11\bar{v}^2 + 69\bar{v}^4 - 45\bar{v}^6}{\bar{v}} + 3\frac{(1-\bar{v}^2)^2(1 - 2\bar{v}^2 - 15\bar{v}^4)}{\bar{v}^2}\log\left(\frac{1-\bar{v}}{1+\bar{v}}\right). \tag{49}$$

For the two-bubble contribution, the first term in Eq. (43) will not vanish (except for $\bar{v} = 1$; see below), so we keep only this term. To lowest order in ϵ, we have

$$\Delta^{(d)}_{HF} = \frac{\pi\epsilon^{-5}\omega_*^2}{24}\int_{-\infty}^{\infty} d\bar{t} \int_{-\infty}^{\bar{t}} dt_N \Gamma(t_N) \int_{-\infty}^{\bar{t}} dt'_N \Gamma(t'_N) \times \int_0^{\infty} dy \cos y \int_{\bar{v}y}^{\infty} \frac{dx}{x^4} e^{-I(\bar{t})} \frac{j_2(x)}{x^2} \times Q_+(s, R, R_-) Q_-(s, R', R_-), \tag{50}$$

with

$$Q_+ = -8\epsilon^3 \bar{R}^3 \bar{v} y (x^2 - \bar{v}^2 y^2),$$
$$Q_- = 8\epsilon^3 \bar{R}'^3 \bar{v} y (x^2 - \bar{v}^2 y^2), \tag{51}$$

which give again an overall factor of $\epsilon = \omega^{-1}$. The integrals with respect to t_N and t'_N affect only the factors $\bar{R}^3$, $\bar{R}'^3$, and give factors $I_3(\bar{t})$. The integrations with respect to x and y can be done analytically again (it is convenient to interchange them), and we obtain

$$\Delta^{(d)}_{HF} = \omega^{-1}\frac{\pi\omega_*^2}{18}\int_{-\infty}^{\infty} d\bar{t} e^{-\frac{4\pi}{3}I_3(\bar{t})} I_3(\bar{t})^2 A^{(d)}(\bar{v}), \tag{52}$$

with

$$A^{(d)}(\bar{v}) = -(1-\bar{v}^2)\left[2\frac{3 + 4\bar{v}^2 - 15\bar{v}^4}{\bar{v}} - 3\frac{(1 + \bar{v}^2 + 3\bar{v}^4 - 5\bar{v}^6)}{\bar{v}^2}\log\left(\frac{1+\bar{v}}{1-\bar{v}}\right)\right]. \tag{53}$$

Notice that this contribution vanishes for $\bar{v} = 1$. Therefore, in the ultrarelativistic limit, the two-bubble contribution falls like ω^{-2}, as observed in the computations of Ref. [122].

This approximation for high frequencies is useful since in this limit the integrals in (32)–(33) become difficult to compute numerically due to the highly oscillatory integrand. We have found only the leading term, but higher orders can be obtained in the same way. To calculate the integrals $I_i(\bar{t})$ and the final integral with respect to $\bar{t}$ in Eqs. (48) and (52), we need to know the nucleation rate $\Gamma(t)$ as well as the wall velocity $v(t)$.

C. Constant velocity

In the case of a constant wall velocity we have $R = v(t - t_N)$, $R' = v(t' - t'_N)$, $R_- = vt_-$, $R_+ = v(t_+ - t_N - t'_N)$, and the expressions simplify significantly. For a nucleation rate of the form (7), it is convenient to use $\omega_* = \omega_b = t_b^{-1}$ as the reference frequency, and to use the dimensionless variables $\tau = (t - t_*)/t_b$, $\tau' = (t' - t_*)/t_b$. Thus, we shall make the change of variables

$$\tau_- = \frac{t_-}{t_b}, \qquad \tau_+ = \frac{t_+ - 2t_*}{t_b}, \qquad \tau_N = \frac{t_N - t_*}{t_b},$$
$$\tau'_N = \frac{t'_N - t_*}{t_b}, \qquad \tau_s = \frac{s}{vt_b} \tag{54}$$

in the integrals of Eqs. (36)–(37), and $\bar{\tau} = \bar{t}/t_b$ in Eqs. (48) and (52).

1. Low frequency

In the single-bubble case, the polynomials P_i given by Eqs. (27)–(29) are homogeneous functions of degree 8, so we have

$$P_i(R_+, R_-, s) = (vt_b)^8 P_i(\tau_+ - 2\tau_N, \tau_-, \tau_s). \tag{55}$$

Changing the order of integration with respect to τ_N and τ_s, we obtain

$$B^{(s)} = \frac{v^3 t_b^3}{48}\int_{-\infty}^{\infty} d\tau_+ \int_0^{\infty} d\tau_- \int_{\tau_-}^{\infty} \frac{d\tau_s}{\tau_s^3} e^{-I_{\rm tot}} \int_{-\infty}^{\frac{\tau_+ - \tau_s}{2}} d\tau_N \tilde{\Gamma}(\tau_N) \times \left[P_0 + \frac{P_1}{3} + \frac{P_2}{15}\right], \tag{56}$$

with P_i evaluated at the dimensionless variables as in the right-hand side of Eq. (55). For the two-bubble case, the polynomials $Q_\pm$, Eqs. (30)–(31), are homogeneous functions of degree 6. Changing the order of integration, we obtain

$$B^{(d)} = \frac{\pi v^3 t_b^3}{48}\int_{-\infty}^{\infty} d\tau_+ \int_0^{\infty} d\tau_- \int_{\tau_-}^{\infty} \frac{d\tau_s}{\tau_s^4} \frac{e^{-I_{\rm tot}}}{15} \times \int_{-\infty}^{\frac{\tau_+ - \tau_s}{2}} d\tau_N \tilde{\Gamma}(\tau_N) Q_+ \int_{-\infty}^{\frac{\tau_+ - \tau_s}{2}} d\tau'_N \tilde{\Gamma}(\tau'_N) Q_-, \tag{57}$$

where the quantities $Q_\pm$ are now given by

$$Q_+(\tau_s, \tau - \tau_N, \tau_-) = (\tau_s^2 - \tau_-^2)[(\tau_+ - 2\tau_N)^2 - \tau_s^2] \times [\tau_s^2 - \tau_-(\tau_+ - 2\tau_N)], \tag{58}$$

$$Q_-(\tau_s, \tau' - \tau'_N, \tau_-) = (\tau_s^2 - \tau_-^2)[(\tau_+ - 2\tau'_N)^2 - \tau_s^2] \times [\tau_s^2 + \tau_-(\tau_+ - 2\tau'_N)]. \tag{59}$$

Finally, for the dimensionless quantities appearing in $I_{\rm tot}$ we have

$$I = \frac{4\pi}{3}\int_{-\infty}^{\tau} d\tau'' \tilde{\Gamma}(\tau'')(\tau - \tau'')^3 \tag{60}$$

and

$$I_\cap = \frac{\pi}{12}\int_{-\infty}^{\frac{\tau_+ - \tau_s}{2}} d\tau'' \tilde{\Gamma}(\tau'')(\tau_+ - 2\tau'' - \tau_s)^2 \times \left[\tau_s + 2(\tau_+ - 2\tau'') - \frac{3\tau_-^2}{\tau_s}\right]. \tag{61}$$

Thus, Eqs. (35)–(37) give

$$\Delta_{LF} = D v^3 \omega^3 / \omega_b^3, \tag{62}$$

with a numerical coefficient $D = (D^{(s)} + \pi D^{(d)})/48$, where $D^{(s)}$ and $D^{(d)}$ are given by the integrals in Eqs. (56) and (57), respectively. By definition, the dimensionless function $\tilde{\Gamma}(\tau)$ does not depend on t_b or v, so the parametric dependence is $\Delta_{LF} \propto v^3 t_b^3 \omega^3$.

2. High frequency

For constant velocity, we have $\bar{v}(\bar{t}) = v$, and the functions $A^{(s)}(v)$ and $A^{(d)}(v)$ do not depend on the integration variable $\bar{t}$ in Eqs. (48) and (52). Using again the dimensionless form of the nucleation rate, Eq. (42) becomes

$$I_n(\bar{t}) = (v t_b)^{n-3}\int_{-\infty}^{\bar{\tau}} d\tau'' \tilde{\Gamma}(\tau'')(\bar{\tau} - \tau'')^n \equiv (v t_b)^{n-3} \tilde{I}_n(\bar{\tau}) \tag{63}$$

Thus, we have

$$\Delta_{HF} = A(v)\omega_b/\omega, \tag{64}$$

with

$$A(v) = C^{(s)} A^{(s)}(v) + C^{(d)} A^{(d)}(v), \tag{65}$$

where the two numerical coefficients $C^{(s)}$ and $C^{(d)}$ are given by

$$C^{(s)} = \frac{\pi}{72}\int_{-\infty}^{\infty} d\bar{\tau} e^{-\frac{4\pi}{3}\tilde{I}_3(\bar{\tau})} \tilde{I}_4(\bar{\tau}) \tilde{I}_2(\bar{\tau}),$$
$$C^{(d)} = \frac{\pi}{18}\int_{-\infty}^{\infty} d\bar{\tau} e^{-\frac{4\pi}{3}\tilde{I}_3(\bar{\tau})} [\tilde{I}_3(\bar{\tau})]^2, \tag{66}$$

and we remark that the functions $A^{(s)}(v)$ and $A^{(d)}(v)$ are given analytically by Eqs. (49) and (53), respectively. For most of the nucleation rates considered below, the coefficients $C^{(s)}$ and $C^{(d)}$ can also be calculated analytically.

3. Interpolation

Although we cannot give an analytic fit for the spectrum for an arbitrary nucleation rate, we note that, from the two asymptotes (62) and (64), we may obtain a rough approximation for the whole spectrum. The intersection of the curves of Δ_{LF} and Δ_{HF} occurs at $\omega = \omega_\times$, $\Delta = \Delta_\times$, with

$$\omega_\times/\omega_b = [A(v)/D v^3]^{1/4}, \qquad \Delta_\times = [D v^3 A(v)^3]^{1/4}. \tag{67}$$

We shall check with specific examples below that these values give the approximate position of the peak frequency ω_p as well as an order-of-magnitude estimate of the amplitude $\Delta(\omega_p)$. The actual value of the latter is below the intersection point, and a better approximation to $\Delta(\omega)$ is given by the simple interpolation

$$\Delta_{\rm int}(\omega) = (\Delta_{LF}^{-1/2} + \Delta_{HF}^{-1/2})^{-2}. \tag{68}$$

The maximum of Eq. (68) is at $\sqrt{3}\omega_\times$, and the value of $\Delta_{\rm int}$ at this frequency is given by $3^{3/2}\Delta_\times/16$. For small velocity we have

$$\frac{\omega_\times}{\omega_b} = 4\left(\frac{C^{(d)} + 4C^{(s)}}{5D}\right)^{\frac{1}{4}} + \mathcal{O}(v^2),$$
$$\Delta_\times = 64 D^{\frac{1}{4}}\left(\frac{C^{(d)} + 4C^{(s)}}{5}\right)^{\frac{3}{4}} v^3 + \mathcal{O}(v^5). \tag{69}$$

Therefore, the peak frequency is approximately fixed for most of the velocity range, while the amplitude is roughly proportional to v^3. Near $v=1$ the intersection point departs from Eq. (69). We have

$$\frac{\omega_\times}{\omega_b} = 2\left(\frac{2C^{(s)}}{D}\right)^{1/4} + \mathcal{O}(1-v),$$
$$\Delta_\times = 8D^{1/4}(2C^{(s)})^{3/4} + \mathcal{O}(1-v). \tag{70}$$

V. SPECIFIC EXAMPLES

We shall now calculate the GW spectrum for a few specific cases. We begin by writing down the expressions for the case of a constant wall velocity. Notice that the expressions for the complete spectrum Δ, Eqs. (32) and (33), are very similar to those for the low-frequency limit, Eqs. (36) and (37). For a constant wall velocity it will be useful to do the same change of variables we used in the previous section, Eq. (54), and we obtain expressions for $\Delta^{(s)}$ and $\Delta^{(d)}$ which are similar to those for $B^{(s)}$ and $B^{(d)}$, Eqs. (56) and (57), but including the factor ω^3 and the oscillating functions shown in Eq. (34). Defining $\tilde{\omega} \equiv \omega/\omega_b$, we have

$$\Delta^{(s)} = \frac{v^3\tilde{\omega}^3}{48}\int_{-\infty}^{\infty} d\tau_+ \int_0^{\infty} d\tau_- \cos(\tilde{\omega}\tau_-) \times \int_{\tau_-}^{\infty} \frac{d\tau_s}{\tau_s^3} \sum_{i=0}^{2} \frac{j_i(v\tilde{\omega}\tau_s)}{(v\tilde{\omega}\tau_s)^i} F_i(\tau_+,\tau_-,\tau_s) e^{-I_{\rm tot}}, \tag{71}$$

where

$$F_i = \int_{-\infty}^{\frac{\tau_+-\tau_s}{2}} d\tau_N \tilde{\Gamma}(\tau_N) P_i(\tau_+ - 2\tau_N, \tau_-, \tau_s), \tag{72}$$

with the polynomials P_i defined in Eqs. (27)–(29), and

$$\Delta^{(d)} = \frac{\pi v^3\tilde{\omega}^3}{48}\int_{-\infty}^{\infty} d\tau_+ \int_0^{\infty} d\tau_- \cos(\tilde{\omega}\tau_-) \times \int_{\tau_-}^{\infty} \frac{d\tau_s}{\tau_s^4} \frac{j_2(v\tilde{\omega}\tau_s)}{(v\tilde{\omega}\tau_s)^2} G_+ G_- e^{-I_{\rm tot}}, \tag{73}$$

where

$$G_\pm(\tau_+,\tau_-,\tau_s) = \int_{-\infty}^{\frac{\tau_+-\tau_s}{2}} d\tau_N \tilde{\Gamma}(\tau_N) Q_\pm\left(\tau_s, \frac{\tau_+ \mp \tau_-}{2} - \tau_N, \tau_-\right). \tag{74}$$

The expressions for the quantities $Q_\pm$ in terms of these variables are given in Eqs. (58) and (59). The quantity $I_{\rm tot}$ is given by Eqs. (60) and (61) as a function of τ_+, τ_-, and τ_s.

A. Exponential nucleation rate

The case of an exponential nucleation rate (and a constant wall velocity) was studied numerically in Refs. [116–118] and analytically in Ref. [122]. We shall now see that Eqs. (71)–(74) give for this case the analytic result of Ref. [122]. We use the parametrization (9) for the nucleation rate, which is of the form (7) with $\tilde{\Gamma}(\tau) = \frac{1}{8\pi}e^{\tau}$, $t_b = \beta^{-1}$, and $v_b = v$. In this case, we have $\omega_b = \beta$, and the dimensionless spectrum (18) (with $\omega_* = \omega_b$) coincides with the expression (17). Since $\tilde{\Gamma}$ is an exponential and P_i, $Q_\pm$ are polynomials, the integrals (72) and (74) are straightforward. We obtain

$$F_i = \frac{2}{\pi} e^{\tau_+/2} e^{-\tau_s/2} \tilde{F}_i(\tau_-,\tau_s),$$
$$G_+ G_- = \frac{1}{4\pi^2} e^{\tau_+} e^{-\tau_s} \tilde{G}(\tau_-,\tau_s)\tilde{G}(-\tau_-,\tau_s), \tag{75}$$

with

$$\tilde{F}_0 = 2(\tau_s^2 + 6\tau_s + 12)(\tau_s^2 - \tau_-^2)^2, \tag{76}$$

$$\tilde{F}_1 = 2(\tau_s^2 - \tau_-^2)[(\tau_s^3 + 4\tau_s^2 + 12\tau_s + 24)\tau_s^2 - (\tau_s^3 + 12\tau_s^2 + 60\tau_s + 120)\tau_-^2], \tag{77}$$

$$\tilde{F}_2 = \frac{1}{2}[(\tau_s^4 + 4\tau_s^3 + 20\tau_s^2 + 72\tau_s + 144)\tau_s^4 + (\tau_s^4 + 20\tau_s^3 + 180\tau_s^2 + 840\tau_s + 1680)\tau_-^4 - (2\tau_s^4 + 24\tau_s^3 + 168\tau_s^2 + 720\tau_s + 1440)\tau_s^2\tau_-^2], \tag{78}$$

$$\tilde{G} = (\tau_s^2 - \tau_-^2)[\tau_s^3 + 2\tau_s^2 - \tau_-(\tau_s^2 + 6\tau_s + 12)]. \tag{79}$$

On the other hand, we have $I(t) = e^{\tau} = e^{(\tau_+-\tau_-)/2}$, $I(t') = e^{\tau'} = e^{(\tau_++\tau_-)/2}$, and $I_\cap = \frac{1}{4}e^{\tau_+/2}e^{-\tau_s/2}(\tau_s + 4 - \tau_-^2/\tau_s)$. Summing these contributions, we obtain

$$I_{\rm tot} = e^{\tau_+/2}[2\cosh(\tau_-/2) - e^{-\tau_s/2}(\tau_s/4 + 1 - \tau_-^2/4\tau_s)]. \tag{80}$$

Notice that, in all these expressions, the variable τ_+ appears only in exponentials $e^{\tau_+/2}, e^{\tau_+}$, and the integration with respect to this variable can be readily done using the substitution $u = e^{\tau_+/2}$. We obtain

$$\Delta^{(s)} = \frac{(v\tilde{\omega})^3}{12\pi}\int_0^{\infty} d\tau_- \cos(\tilde{\omega}\tau_-) \int_{\tau_-}^{\infty} \frac{d\tau_s}{\tau_s^3} \times \frac{\tilde{F}_0 j_0(v\tilde{\omega}\tau_s) + \tilde{F}_1 \frac{j_1(v\tilde{\omega}\tau_s)}{v\tilde{\omega}\tau_s} + \tilde{F}_2 \frac{j_2(v\tilde{\omega}\tau_s)}{(v\tilde{\omega}\tau_s)^2}}{2\cosh(\frac{\tau_-}{2})e^{\frac{\tau_s}{2}} - 1 - (\tau_s^2 - \tau_-^2)/4\tau_s}, \tag{81}$$

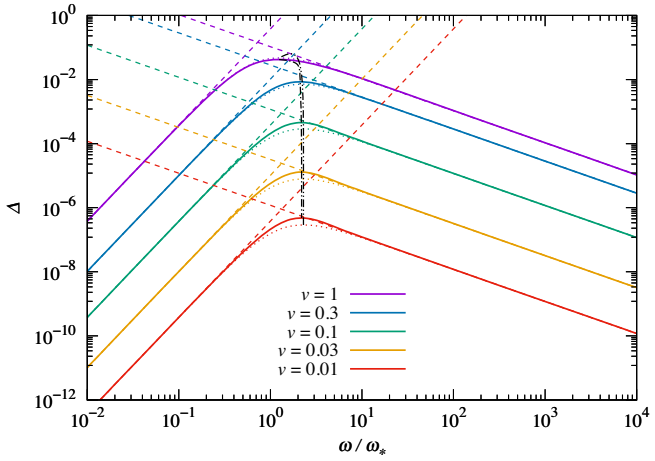

FIG. 1. The GW spectrum for the exponential nucleation rate, with $\omega_* = \beta$ (solid lines). The dashed lines indicate the asymptotes, and the dotted lines correspond to the interpolation (68). The dash-dot lines indicate the peak values (ω_p, Δ_p) for the spectrum, and dash-dot-dot lines those for the interpolation.

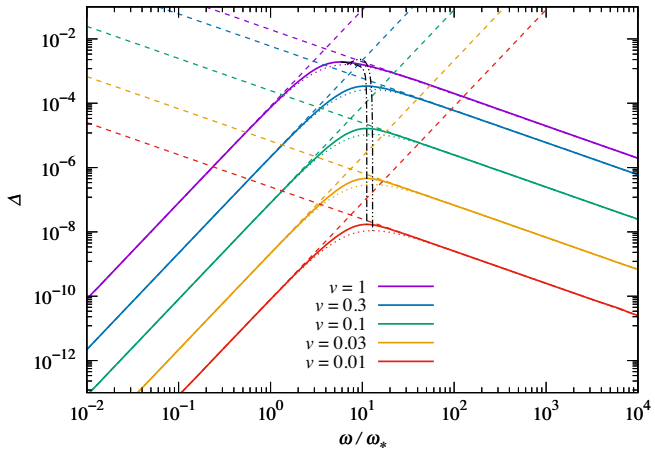

FIG. 2. Like Fig. 1 but for the delta-function rate, with $\omega_* = v/d_b$.

$$\Delta^{(d)} = \frac{(v\tilde{\omega})^3}{96\pi} \int_0^\infty d\tau_- \cos(\tilde{\omega}\tau_-) \int_{\tau_-}^\infty \frac{d\tau_s}{\tau_s^4} \times \frac{\tilde{G}(\tau_-, \tau_s)\tilde{G}(-\tau_-, \tau_s) \frac{j_2(v\tilde{\omega}\tau_s)}{(v\tilde{\omega}\tau_s)^2}}{[2\cosh(\frac{\tau_-}{2})e^{\frac{\tau_s}{2}} - 1 - (\tau_s^2 - \tau_-^2)/4\tau_s]^2}, \tag{82}$$

in agreement with Ref. [122].

In Fig. 1 we plot the spectrum for several wall velocities, as well as the low-frequency and high-frequency approximations Δ_{LF}, Δ_{HF} given by Eqs. (62) and (64), respectively. The coefficients for these approximations are[10] $D \simeq 0.3820$, $C^{(s)} = (96\pi)^{-1}$, and $C^{(d)} = (32\pi)^{-1}$. We see that the asymptotic curves give an order-of-magnitude approximation in the whole range. The figure also shows the simple interpolation (68). Its maximum gives a good approximation for the peak frequency, $\omega_p \simeq \sqrt{3}\omega_\times$. The error is less than 10% for all the curves. On the other hand, the maximum value of Δ for the interpolation gives a rough approximation for the peak amplitude, $\Delta_p \simeq 3^{3/2}\Delta_\times/16$, although for some of the curves this value departs more than 50% from the actual value.

B. Simultaneous nucleation

We now calculate the GW spectrum for a delta-function nucleation rate. This case was considered in Ref. [126] as a limit of a Gaussian nucleation rate. In that work, the general expressions (B.22) and (B.28) have the same form of our Eqs. (71)–(73). However, their specific expressions for the integrands, Eqs. (B.30)–(B.36), are somewhat cumbersome for a direct comparison. On the other hand, we shall perform the integral with respect to τ_- analytically, which greatly simplifies the remaining numerical integrations and will allow us to consider a much wider frequency range. The particular case $v = 1$ was considered also in Ref. [118]. In Appendix C we compare the different numerical results.

We use the parametrization (14) of the nucleation rate, for which the dimensionless rate is $\tilde{\Gamma}(\tau) = \delta(\tau)$ and the timescale is defined as $t_b = d_b/v$. The associated frequency is $\omega_b = t_b^{-1} = v/d_b$, and we shall use this as the reference frequency ω_* for the dimensionless spectrum Δ. Due to the delta function, the integrals (72) and (74) are trivial, and we obtain

$$\begin{aligned} F_i &= P_i(\tau_+, \tau_-, \tau_s)\Theta(\tau_+ - \tau_s), \\ G_- G_+ &= Q(\tau_+, \tau_-, \tau_s)\Theta(\tau_+ - \tau_s), \end{aligned} \tag{83}$$

where P_i are the polynomials defined in Eqs. (27)–(29), and

$$Q = (\tau_+^2 - \tau_s^2)^2(\tau_s^2 - \tau_-^2)^2(\tau_s^4 - \tau_-^2\tau_+^2). \tag{84}$$

Hence, Eqs. (71) and (73) become

$$\Delta^{(s)} = \frac{v^3\tilde{\omega}^3}{48} \int_0^\infty d\tau_+ \int_0^{\tau_+} d\tau_- \cos(\tilde{\omega}\tau_-) \times \int_{\tau_-}^{\tau_+} \frac{d\tau_s}{\tau_s^3} \sum_{i=0}^{2} \frac{j_i(v\tilde{\omega}\tau_s)}{(v\tilde{\omega}\tau_s)^i} P_i(\tau_+, \tau_-, \tau_s) e^{-I_{\rm tot}}, \tag{85}$$

$$\Delta^{(d)} = \frac{\pi v^3\tilde{\omega}^3}{48} \int_0^\infty d\tau_+ \int_0^{\tau_+} d\tau_- \cos(\tilde{\omega}\tau_-) \times \int_{\tau_-}^{\tau_+} \frac{d\tau_s}{\tau_s^4} \frac{j_2(v\tilde{\omega}\tau_s)}{(v\tilde{\omega}\tau_s)^2} Q(\tau_+, \tau_-, \tau_s) e^{-I_{\rm tot}}, \tag{86}$$

The integrals for $I_{\rm tot}$ are also trivial, and we obtain

[10]The functions $\tilde{I}_n(\bar{\tau})$ defined in Eq. (63) are given by $\tilde{I}_2 = \frac{1}{4\pi}e^{\bar{\tau}}$, $\tilde{I}_3 = \frac{3}{4\pi}e^{\bar{\tau}}$, and $\tilde{I}_4 = \frac{3}{\pi}e^{\bar{\tau}}$.

$$I_{\rm tot} = \frac{\pi}{12}(2\tau_+^3 - \tau_s^3 + 3\tau_+^2\tau_s) + \frac{\pi}{4}\frac{(\tau_+ + \tau_s)^2}{\tau_s}\tau_-^2 \qquad (87)$$

Since the exponent (87) is quadratic in τ_-, the integrals with respect to this variable can be calculated analytically. We must first interchange the integrals with respect to τ_- and τ_s using $\int_0^{\tau_+} d\tau_- \int_{\tau_-}^{\tau_+} d\tau_s = \int_0^{\tau_+} d\tau_s \int_0^{\tau_s} d\tau_-$. We obtain

$$\Delta^{(s)} = \frac{(v\tilde{\omega})^3}{48}\int_0^\infty d\tau_+ \int_0^{\tau_+} \frac{d\tau_s}{\tau_s^3} e^{-\frac{\pi}{12}(2\tau_+^3 - \tau_s^3 + 3\tau_+^2\tau_s)} \times \sum_{i=0}^{2} \frac{j_i(v\tilde{\omega}\tau_s)}{(v\tilde{\omega}\tau_s)^i}\tilde{P}_i(\tau_+, \tau_s, \tilde{\omega}), \qquad (88)$$

with

$$\tilde{P}_i(\tau_+, \tau_s, \tilde{\omega}) = \int_0^{\tau_s} d\tau_- \cos(\tilde{\omega}\tau_-) P_i(\tau_+, \tau_-, \tau_s) e^{-\frac{\pi}{4}\frac{(\tau_+ + \tau_s)^2}{\tau_s}\tau_-^2}, \qquad (89)$$

and

$$\Delta^{(d)} = \frac{\pi(v\tilde{\omega})^3}{48}\int_0^\infty d\tau_+ \int_0^{\tau_+} \frac{d\tau_s}{\tau_s^4} e^{-\frac{\pi}{12}(2\tau_+^3 - \tau_s^3 + 3\tau_+^2\tau_s)} \frac{j_2(v\tilde{\omega}\tau_s)}{(v\tilde{\omega}\tau_s)^2} \times \tilde{Q}(\tau_+, \tau_s, \tilde{\omega}), \qquad (90)$$

with

$$\tilde{Q}(\tau_+, \tau_s, \tilde{\omega}) = \int_0^{\tau_s} d\tau_- \cos(\tilde{\omega}\tau_-) Q(\tau_+, \tau_-, \tau_s) e^{-\frac{\pi}{4}\frac{(\tau_+ + \tau_s)^2}{\tau_s}\tau_-^2}. \qquad (91)$$

The analytic expressions for the functions $\tilde{P}_i$ and $\tilde{Q}$ are given in Appendix A.

In Appendix A we plot separately the single-bubble and the two-bubble contributions to the GW spectrum. In Fig. 2 we plot the complete spectrum together with the asympotic curves and the interpolation. The coefficient of the low frequency approximation is $D \simeq 8.066 \times 10^{-5}$, while those of the high-frequency approximation are given by[11]

$$C^{(s)} = \frac{\Gamma(7/3)}{128\pi^{4/3}6^{2/3}} \simeq 6.123 \times 10^{-4},$$
$$C^{(d)} = \frac{\Gamma(7/3)}{32\pi^{4/3}6^{2/3}} \simeq 2.449 \times 10^{-3}. \qquad (92)$$

We see that, at the maximum, the interpolations are not as good approximations as in the previous case. The peak frequency departs more than 50% and the amplitude departs by a factor of 2 in some cases.

[11]The functions $\tilde{I}_n(\bar{\tau})$ which appear in the expressions for $C^{(s)}$ and $C^{(d)}$ are given by $\tilde{I}_n = \bar{\tau}^n$.

C. Gaussian nucleation rate

We shall now consider a nucleation rate of the form $e^{-\gamma^2(t-t_m)^2}$. A Gaussian nucleation rate was considered in Ref. [126] with a different parametrization, namely, $e^{\beta(t-t_*)-\gamma^2(t-t_*)^2}$. This parametrization is useful when the phase transition occurs away from the maximum of the Gaussian (in particular, it allows to consider the case $\gamma = 0$), while we are more interested in the case in which the phase transition occurs around this maximum. For a given physical model, the two exponents correspond to the expansion of $S(t)$ around two different times t_m, t_*. Therefore, the value of γ is different in each case. We compare the two approaches in more detail in Appendix B.

We shall use the parametrization (13), which is of the form (7), with t_b replaced by the parameter $t_{\rm min}$ for simplicity of the expressions. The dimensionless rate is $\tilde{\Gamma}(\tau) = (\alpha/\sqrt{\pi})e^{-(\alpha\tau)^2}$, where $\alpha = \gamma t_{\rm min}$. The timescale of the nucleation rate is $t_\Gamma \sim \gamma^{-1}$, but the duration of the phase transition, t_b, depends mainly on the value of $t_{\rm min}$. We shall use the reference frequency $\omega_* = t_{\rm min}^{-1}$, so the dimensionless spectrum is given by Eqs. (71)–(74), with $\tilde{\omega} = \omega/t_{\rm min}^{-1}$.

The integrals (72) and (74) can be done analytically. The expressions for F_i and $G_\pm$ contain polynomials, the Gaussian function, and the error function. These expressions are rather cumbersome, and we write them down in Appendix B. The function $I_{\rm tot}$ also contains error functions which depend on the variables t_-, t_+, t_s, so the remaining integrals in Eqs. (71) and (73) cannot be done analytically. The multiple integration is difficult to do numerically, and in Ref. [126] a limited frequency range around the peak of the spectrum was considered. In particular, the high frequency behavior cannot be seen in those results. Therefore, this case provides an example of the usefulness of our asymptotic approximations. In Fig. 3 we show the spectrum, the asymptotes, and the interpolation for the case $\alpha = 1$ and for several values of the wall velocity. We give

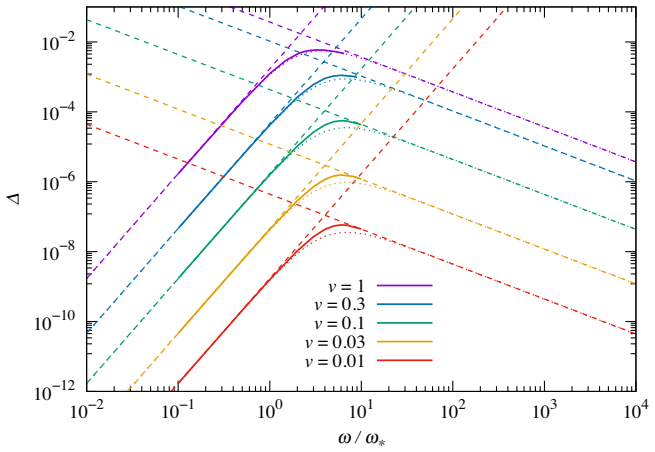

FIG. 3. Like Fig. 1 but for a Gaussian nucleation rate with $\alpha = 1$. Here, $\omega_* = t_{\rm min}^{-1}$.

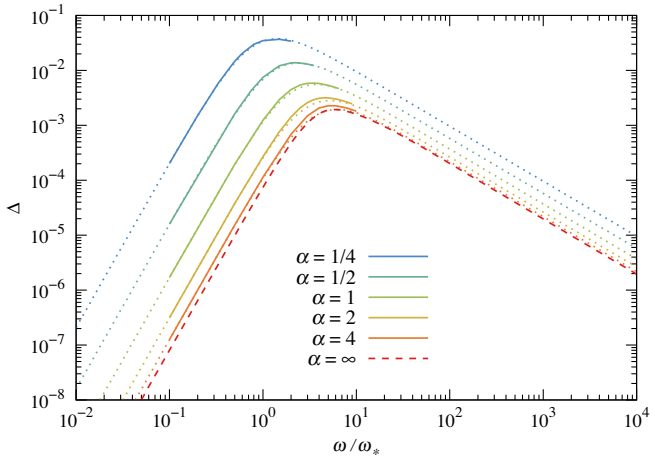

FIG. 4. The spectrum (solid lines) and the interpolation approximation (dotted lines) for the Gaussian nucleation rate for $v = 1$, with $\omega_* = t_{\rm min}^{-1}$. The dashed line corresponds to the delta-function rate.

the details of the calculation in Appendix B. We have computed the exact GW spectrum only in the range $0.1 \leq \omega/\omega_* \lesssim 10$. For higher frequencies, the multiple integration becomes very difficult due to the highly oscillating integrand. Nevertheless, we see that in this case the high-frequency asymptote or the interpolation become good approximations. For lower frequencies, the numerical integration does not present critical difficulties. In any case, we see that for $\omega/\omega_* \sim 10^{-1}$ the low-frequency asymptote is already a very good approximation.

In Fig. 4 we show the GW spectrum for a few values of the parameter α. The dashed red curve actually corresponds to the simultaneous nucleation considered in the previous subsection. Indeed, in the limit of large α we have $t_\Gamma \ll t_{\rm min}$, and the Gaussian becomes a delta function. The opposite limit, $\alpha \to 0$, corresponds to $t_{\rm min} \ll t_\Gamma$, but in this case $t_{\rm min}$ does not represent the duration of the phase transition, i.e., we have $t_b > t_{\rm min}$. We discuss the dependence with the timescales in the next section. Notice also that the limit $\alpha \to 0$ can be interpreted as $\gamma \to 0$. However, this limit does not coincide with what is usually called a constant nucleation rate. The latter is actually a Heaviside function since it turns on at a given time t_0. We consider this case next.

D. Constant nucleation rate

Although a constant nucleation rate $\Gamma_0\Theta(t - t_0)$ is not well motivated physically, we shall discuss it here since it is often used as an approximation (for its application to the computation of GWs, see [120]). We use the parametrization (8) for the nucleation rate, so we have $\tilde{\Gamma}(\tau) = \frac{3}{\pi}\Theta(\tau)$, and we compute the dimensionless spectrum (18) with $\omega_* = \omega_b = t_b^{-1}$, which is given by Eqs. (71)–(74). In this case, the integrands in Eqs. (72) and (74) are polynomials, and we obtain, omitting a Heaviside $\Theta(\tau_+ - \tau_s)$ in the expressions,

$$F_0 = \frac{1}{10\pi}(\tau_+ - \tau_s)^3(\tau_-^2 - \tau_s^2)^2(3\tau_+^2 + 9\tau_+\tau_s + 8\tau_s^2), \tag{93}$$

$$F_1 = \frac{1}{5\pi}(\tau_s^2 - \tau_-^2)[15\tau_+\tau_-^2(\tau_+^2 - \tau_s^2)^2 + \tau_s^2\tau_+(45\tau_s^4 - 10\tau_+^2\tau_s^2 - 3\tau_+^4) - 32\tau_s^7], \tag{94}$$

$$F_2 = \frac{1}{10\pi}[15\tau_-^4\tau_+(7\tau_+^4 - 10\tau_+^2\tau_s^2 + 3\tau_s^4) + 30\tau_-^2\tau_s^2\tau_+(\tau_s^4 + 2\tau_+^2\tau_s^2 - 3\tau_+^4) \tag{95}$$

$$+\tau_s^4\tau_+(9\tau_+^4 + 10\tau_+^2\tau_s^2 + 45\tau_s^4) - 64\tau_s^9], \tag{96}$$

$$G_\pm = \mp\frac{1}{8\pi}(\tau_+ - \tau_s)^2(\tau_s^2 - \tau_-^2) \times [3\tau_-(\tau_+ + \tau_s)^2 \mp 4\tau_s^2(\tau_+ + 2\tau_s)]. \tag{97}$$

On the other hand, we have $I = \tau^4$, $I_\cap = \frac{1}{16}(\tau_+ - \tau_s)^3(\tau_+ + \tau_s - 2\tau_-^2/\tau_s)$, and

$$I_{\rm tot} = \frac{1}{16}[(\tau_+ - \tau_-)^4 + (\tau_+ + \tau_-)^4 - (\tau_+ - \tau_s)^3(\tau_+ + \tau_s - 2\tau_-^2/\tau_s)] \tag{98}$$

The remaining integrals with respect to τ_+, τ_-, and τ_s in Eqs. (71) and (73) cannot be done analytically.

In Fig. 5 we show the spectrum, the asymptotes, and the interpolation, for several values of the wall velocity. The coefficient of the low-frequency approximation (62) is given by

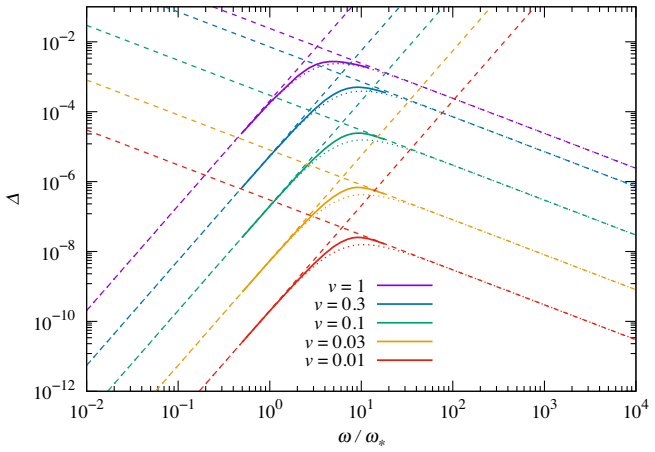

FIG. 5. Like Fig. 1 but for a constant nucleation rate, with $\omega_* = t_b^{-1}$.

$$D = \frac{1}{48}\int_{-\infty}^{\infty} d\tau_+ \int_0^{\infty} d\tau_- \int_{\tau_-}^{\tau_+} \frac{d\tau_s}{\tau_s^3} e^{-I_{\rm tot}} \times \left[F_0 + \frac{F_1}{3} + \frac{F_2}{15} + \frac{\pi G_+ G_-}{15\tau_s}\right] \simeq 2.046 \times 10^{-4}. \quad (99)$$

For the high-frequency approximation (64)–(65), the coefficients are given by[12]

$$C^{(s)} = \frac{\Gamma(9/4)}{480\pi} \simeq 7.513 \times 10^{-4}, \qquad C^{(d)} = \frac{\Gamma(9/4)}{128\pi} \simeq 2.818 \times 10^{-3}. \quad (100)$$

The case $v = 1$ can be compared with the lattice simulations of Ref. [120]. We find that the peak for envelope approximation is slightly to the left with respect to that computation. We discuss the differences between these approaches in Sec. VII.

VI. TIME AND SIZE SCALES

It has been discussed in the literature whether the GWs should inherit the characteristic frequency or the characteristic length of the source (see, e.g., [98–100,144]). This issue was specifically analyzed in Ref. [145]. For a spatially homogeneous and short lived source, the GWs are expected to inherit the characteristic length. However, for the bubble collision mechanism, it turns out that the characteristic frequency is of the order of the timescale t_b rather than the length scale $d_b = vt_b$. This was observed numerically for the exponential rate in Refs. [117,122], and can be seen in all the plots of the previous section, where the peak frequency ω_p is around the value $\omega_* \sim t_b^{-1}$. Below we discuss this issue in more detail.

A. The bubble size distribution

Some of the cases considered above correspond to very different bubble size distributions. For instance, for an exponential nucleation, smaller bubbles, which nucleate later, have exponentially higher number densities than larger bubbles, which nucleate earlier. Besides, newer bubbles only nucleate in the increasingly smaller regions remaining in the false vacuum, so the space distribution also depends on the bubble size. In contrast, for a simultaneous nucleation, all the bubbles have the same size at any time during the phase transition. However, the shape of the spectrum is very similar for the two nucleation rates. This can be seen more clearly in Fig. 12 in Appendix C. Therefore, the presence of different size scales does not seem to be relevant for GW production.

As argued in Ref. [117], the result $\omega_p \sim t_b^{-1}$ may be explained by the fact that, for $v \ll 1$, the duration of the phase transition is not actually short in comparison to the scale $d_b = vt_b$. Hence, the GWs do not inherit the distance scale. This explains also why the size distribution is not a decisive factor.

Notice, indeed, that the relevant bubble radius is *at most* of order vt_b. This is quite clear for a simultaneous nucleation, since the bubble radius is limited by the bubble separation d_b and the time of bubble expansion is $\sim d_b/v$. In the exponential case, the average radius at any time is approximately given by $v\beta^{-1}$, and the width of the radius distribution is of the same order. Since the released energy is proportional to the bubble volume, it is sometimes assumed that the volume distribution of bubbles is the relevant quantity [116]. This quantity also has its peak at a radius of order $v\beta^{-1}$.

One could argue that, since the walls of different bubbles join to form larger domains, in the evolution of this system of walls, there will be length scales which are larger than vt_b (at percolation, there will be domains of size H^{-1}). However, the spatial correlation within these domains falls rapidly beyond a distance of the order of the typical bubble radius [135], so we do not expect a relevant length scale beyond this distance. Moreover, for the single-bubble contribution, any length scale involved is of order vt_b or smaller, so the timescale is the relevant quantity. Indeed, this contribution alone has a peak at $\omega \sim t_b^{-1}$ rather than at $\omega \sim d_b^{-1}$ (see Fig. 10 in Appendix A for the simultaneous case or Ref. [122] for the exponential case).

B. Model comparison

Since two different nucleation rates depend on different kinds of parameters, for a sensible comparison it is necessary to fix some physical quantity. For the exponential and delta-function cases, the final average bubble separation $d_b \equiv n_b^{-1/3}$ has often been used for such a purpose (see, e.g., [118,120]). For the simultaneous nucleation, this is just a parameter of the nucleation rate, while for the exponential nucleation it is given by

$$d_b = (8\pi)^{1/3} v/\beta, \quad (101)$$

If we fix a different physical quantity, the comparison will be quantitatively different. For instance, we may compare an exponential nucleation and a simultaneous nucleation for which the phase transition has the same duration. We may take, as an estimation, the time $\Delta t = t_2 - t_1$ between the moment t_1 at which $f_+ = 0.99$ and t_2 at which $f_+ = 0.01$ [135]. We have $I(t_1) = -\log(0.99) \equiv I_1$ and $I(t_2) = -\log(0.01) \equiv I_2$. For the exponential nucleation rate this quantity is given by

$$\Delta t = (\log I_2 - \log I_1)\beta^{-1} \simeq 6.13\beta^{-1}, \quad (102)$$

[12]In this case we have $\tilde{I}_n(\bar{\tau}) = \frac{3}{(n+1)\pi}\bar{\tau}^{n+1}$.

while for the simultaneous nucleation it is given by

$$\Delta t = (3/4\pi)^{1/3}(I_2^{1/3} - I_1^{1/3})(d_b/v) \simeq 0.898(d_b/v). \tag{103}$$

For the same Δt, the relation between the parameters of these models is

$$d_b = \left(\frac{4\pi}{3}\right)^{1/3} \frac{\log I_2 - \log I_1}{I_2^{1/3} - I_1^{1/3}} \frac{v}{\beta} \tag{104}$$

instead of (101).

In Fig. 6 we compare the two models fixing either d_b or Δt. We need to use the same unit of frequency for all the curves, and we chose $\omega_* = \beta$. The dimensionless spectrum Δ is also normalized using $\omega_* = \beta$ in Eq. (18), which thus coincides with Eq. (17). We consider an exponential nucleation rate (solid lines), a simultaneous nucleation with d_b given by Eq. (101) (dashed lines), and a simultaneous nucleation with d_b given by Eq. (104) (dotted lines), for three different values of the wall velocity. The fact that there is not a unique way of comparing two different nucleation rates implies that the position of the peak for the simultaneous case can be either to the left or to the right of the peak for the exponential case, depending on the quantity which is fixed in the comparison. Similarly, the peak amplitude can be higher or lower.

For a given wall velocity, we see that the GW spectrum for an exponential nucleation is quite closer to that for a simultaneous nucleation with the same value of Δt than to one with the same value of d_b. This seems to be another indication of the fact that, for the bubble collision mechanism, the timescale is more relevant than the length scale. Furthermore, we verify that the peak frequency ω_p is within

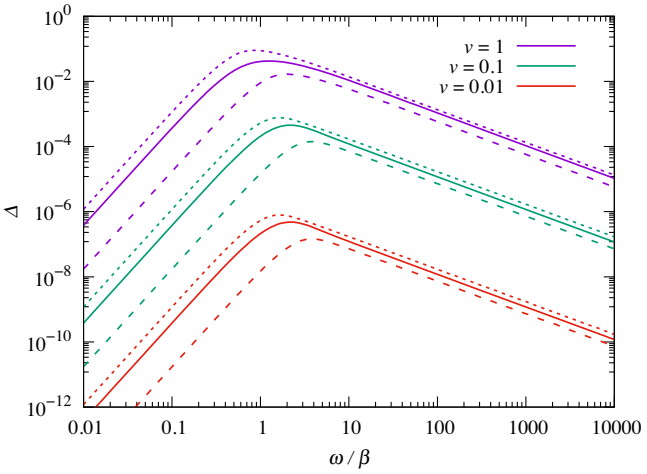

FIG. 6. The GW spectrum for an exponential nucleation rate (solid lines), a delta-function nucleation rate with parameter d_b given by Eq. (101) (dashed lines), and a delta-function rate with d_b given by Eq. (104) (dotted lines).

the range $(1-3)\beta$ for all the curves in Fig. 6, while $d_b \sim v\beta^{-1}$ varies by two orders of magnitude for the velocity range considered in the figure. On the other hand, the amplitude Δ_p does vary with the distance scale. According to Fig. 6, we have, roughly, $\Delta_p \sim d_b^3$.

This behavior can be seen analytically for an arbitrary nucleation rate from the approximation $\omega_p \simeq \sqrt{3}\omega_\times$, where $\omega_\times$ is proportional to $\omega_b = t_b^{-1}$. According to Eqs. (69) and (70), as a function of the velocity, the ratio $\omega_\times/\omega_b$ varies between two $\mathcal{O}(1)$ values (below we discuss the Gaussian case, where the dimensionless coefficients in these equations depend on the ratio between two timescales). Hence, the behavior $\omega_p \sim \omega_\times \sim t_b^{-1}$ is quite model independent. For the peak amplitude, we have $\Delta_p \sim \Delta_\times$, which is roughly $\propto v^3$.

C. Two timescales

The Gaussian nucleation rate $\Gamma = \Gamma_m e^{-\gamma^2(t-t_m)^2}$ provides a model with two different timescales, since the time during which bubble nucleation is active does not necessarily coincide with the duration of the phase transition. We have defined two time parameters, namely, the width of the Gaussian, $t_\Gamma \equiv \gamma^{-1}$, and the time associated to the minimal bubble separation $t_{\min} = d_{\min}/v$. The latter is obtained from $\Gamma(t)$ alone, i.e., omitting the suppression factor f_+ in Eq. (5), and is given by $d_{\min} = (\sqrt{\pi}\Gamma_m/\gamma)^{-1/3}$. We remark that the use of the parameters t_Γ, $t_{\min}$ is convenient due to their simple analytical relations with the parameters γ and Γ_m. As we discuss in Appendix B, in the cases in which the phase transition actually occurs around the maximum of the Gaussian, t_Γ is directly related to the duration of bubble nucleation and $t_{\min}$ is related to the total duration of the phase transition. Otherwise, the nucleation rate can be approximated by an exponential and there is a single timescale which is not simply related to these parameters.

In Sec. V C we used $\omega_* = t_{\min}^{-1}$ as the unit of frequency and we considered different values of the ratio $\alpha = t_{\min}/t_\Gamma$. This means that the different curves in Figs. 3 and 4 correspond to different phase transitions with the same value of $t_{\min}$. In the left panel of Fig. 7 we consider again the curves of Fig. 4. Here we use the interpolation approximation, so that it is easier to reach wider ranges for ω and α. The central panel shows the same spectra with t_Γ^{-1} as the unit of frequency. Therefore, in these curves this timescale is fixed while the parameter $t_{\min}$ varies. We see that the order of the curves is inverted with respect to those in the left panel. Like in Fig. 6, this shows that, when we compare different models (in this case, different values of α), the result depends on which physical quantity we fix in the comparison. In the third panel of Fig. 7 we fix the parameter $t_b = d_b/v$, where d_b is the real bubble separation, i.e., taking into account the factor f_+ in Eq. (5). Therefore, t_b is related to the actual duration of the phase transition. We see that the peak frequency changes very

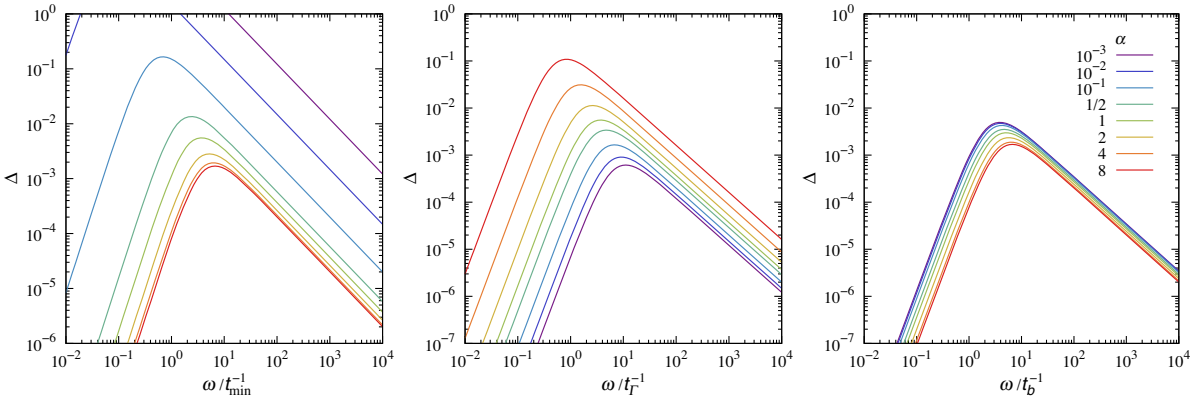

FIG. 7. The spectrum (using the interpolation approximation) for the Gaussian nucleation rate, for $v = 1$. In the left panel we fix the parameter $t_{\min}$, in the central panel we fix the parameter t_Γ, and in the right panel we fix the parameter t_b.

little in this case (we have $4 \lesssim \omega_p/\omega_* \lesssim 6$ for the whole range of α), indicating that ω_p is mostly determined by this timescale.

As already mentioned, in the limit $\alpha \to \infty$ the width of the Gaussian becomes very small in comparison with the duration of the phase transition ($t_\Gamma \ll t_{\min} < t_b$), and we have a simultaneous nucleation. Also, we have $t_{\min} \to t_b$ in this limit. The convergence to the simultaneous case can be seen in the left and right panels of Fig. 7, but not in the central panel, where we normalize the frequency and amplitude using t_Γ^{-1}. On the other hand, in the right panel we also observe a limiting curve for $\alpha \to 0$. In this limit we have $t_{\min} \ll t_\Gamma$, but in this case none of these parameters correspond to a physical time in the evolution of the phase transition. This limit is obtained for $\gamma \to 0$ or $\Gamma_m \to \infty$. Since the nucleation rate acts from $t = -\infty$, this means that in this case the phase transition will be completed about a time t_* much earlier than t_m. Around the time t_* the usual exponential approximation can be used, and the limiting curve corresponds to an exponential nucleation rate (see App. B for more details). Since the value of d_b is fixed in the right panel of Fig. 7, the parameter of the exponential is given by $\beta = (8\pi)^{1/3} v/d_b$.

In Fig. 8 we indicate this limiting curve with a dashed line, and the limit for $\alpha \to \infty$ with a dotted line. We also consider different values of the wall velocity, and we observe again that the peak frequency is always determined by the timescale t_b, while the peak amplitude depends on the length scale $d_b = v t_b$. For a given wall velocity v and a given average separation d_b, the spectrum has larger amplitudes and smaller frequencies in the limit of an exponential nucleation, while it shifts to smaller amplitudes and higher frequencies as we approach the limit of a simultaneous nucleation. Since larger bubbles contribute more than smaller ones to the GW spectrum, this behavior may be due to the differences in the bubble size distribution for the different nucleation rates. Indeed, in the simultaneous case all bubbles have similar sizes, while in the exponential case there are bubbles with sizes much larger than the average. The same behavior can be expected for other mechanisms, such as sound waves. Hence, the differences observed in this figure may be regarded as a quantitative estimate of the degree of error in the spectrum when different nucleation rates are adopted for simplicity in a simulation.

D. Relation with the surface area

Since the characteristic frequency of the gravitational waves is determined by the timescale of the source, it is useful to consider the time evolution of the latter. For the envelope approximation it is clear that the source of GWs is the motion of thin walls. More generally, for any mechanism associated to the bubble walls, the GW production will be weighted by the amount of bubble wall which is present at a given time (as can be seen from the general expressions derived in Ref. [125]). One may wonder

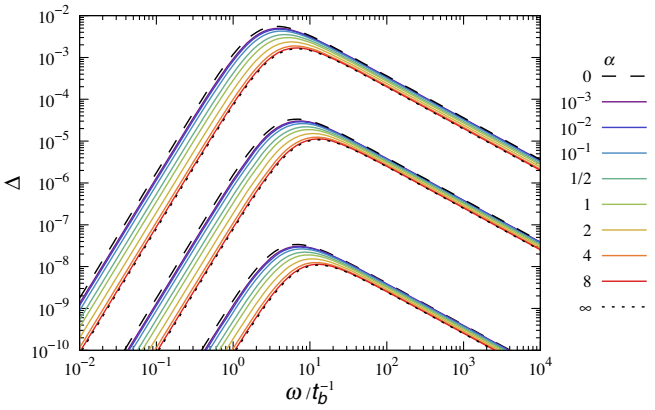

FIG. 8. The spectrum (using the interpolation approximation) for the Gaussian nucleation rate, for different values of α and v. The reference frequency is $\omega_* = t_b^{-1}$. The three groups of curves correspond to velocities $v = 1$, 0.1, and 0.01 from top to bottom. The dotted lines indicate the limit $\alpha \to \infty$ (simultaneous nucleation), and the dashed lines indicate the limit $\alpha \to 0$ (exponential nucleation).

whether the relevant quantity here is the average uncollided wall area, $\langle S\rangle \sim R^2 f_+ \sim R^2 e^{-4\pi R^3/3}$, or the surface energy $\sigma\langle S\rangle \sim R^3 e^{-4\pi R^3/3}$ (since $\sigma \propto R$ due to the release of latent heat), or some other quantity. In the envelope approximation, the energy-momentum tensor is given by Eq. (21), $T_{ij} = \sigma\delta(r-R)\hat{r}_i\hat{r}_j 1_S(\hat{r})$. Since $\langle 1_S\rangle = \langle S\rangle/4\pi R^2$, this seems to indicate that the "effective" surface energy density $\sigma\langle S\rangle/R^2 \sim Re^{-4\pi R^3/3}$ is the relevant quantity. Let us consider for simplicity the case of simultaneous nucleation, for which the above expressions are exact since all the bubbles have the same radius. For instance, the average uncollided wall area of a bubble is just given by

$$\begin{aligned}\langle S\rangle &= 4\pi R^2 e^{-\frac{4\pi}{3}R^3} \\ &= 4\pi d_b^2\left(\frac{t-t_*}{t_b}\right)^2 \exp\left[-\frac{4\pi}{3}\left(\frac{t-t_*}{t_b}\right)^3\right],\end{aligned} \tag{105}$$

and the total uncollided wall area per unit volume is given by $n_b\langle S\rangle = d_b^{-3}\langle S\rangle$. We observe a qualitative relation between this quantity and the GW spectrum, namely, that the time variation is determined by t_b, while the amplitude is determined by the characteristic d_b. Notice, however, that the GW spectrum involves the correlator $\langle T_{ij}T_{kl}{}'\rangle$. For a given bubble, any of the quantities discussed above is of the form $R^n S$, and we should expect that the result depends on $R^n R'^n\langle SS'\rangle$, i.e., that the relevant quantity is the surface correlation rather than $\langle S\rangle$.

In the expression for T_{ij}, the time independent factor $\hat{r}_i\hat{r}_j$ characterizes the spatial dependence of the source (the spherical wall), while the time dependence is contained essentially in the variation of the bubble radius R and the uncollided surface S. If we omit the factor $\Lambda_{ij,kl}\hat{r}_i\hat{r}_j\hat{r}_k{}'\hat{r}_l{}'$ in Eq. (20), and consider for simplicity only the single-bubble contribution, we obtain the rough estimation

$$\begin{aligned}\Pi(t,t',\omega) &\sim n_b\sigma\sigma'\langle S(t)S(t')\rangle \\ &\sim n_b(\kappa\rho_{\rm vac})^2 RR'\langle S(t)S(t')\rangle.\end{aligned} \tag{106}$$

In Ref. [135] it was argued that an estimation for the GW spectrum can be obtained by assuming that the quantity $\Pi(t,t',\omega)$ is proportional to the surface correlator $\langle S(t)S(t')\rangle$. This is equivalent to the further approximation $R \sim R' \sim d_b$ in Eq. (106). For the simultaneous case and the single bubble contribution we have [135]

$$\langle S(t)S(t')\rangle = 8\pi^2 RR'\int_{R'-R}^{R'+R} ds\, s e^{-I_{\rm tot}(t,t',s)}. \tag{107}$$

(notice that this quantity contains information about the correlation between points on the bubble surface). Proceeding as before, for the approximation (106) we obtain

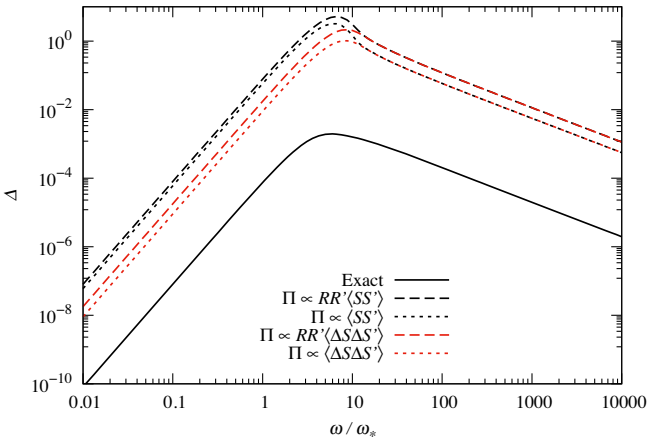

FIG. 9. The GW spectrum and some rough approximations, for a simultaneous nucleation and $v = 1$ ($\omega_* = v/d_b$).

$$\begin{aligned}\Delta \sim v^3\tilde{\omega}^3\int_0^\infty d\tau_+\int_0^{\tau_+} d\tau_s\tau_s\int_0^{\tau_s} d\tau_-\cos(\tilde{\omega}\tau_-)(\tau_+^2-\tau_-^2)^2 \\ \times e^{-I_{\rm tot}(\tau_+,\tau_-,\tau_s)}.\end{aligned} \tag{108}$$

The integrand does not depend on the velocity, so we have an amplitude proportional to v^3 and a shape which depends on $\tilde{\omega} = \omega t_b$. The computation of Eq. (108) is much simpler than the complete expression (88) (see Appendix A). We show the result in Fig. 9 for $v = 1$ (dashed black line). The approximation gives the correct power-law form.[13] The peak intensity, though, is a few orders of magnitude higher than the exact result (solid line). This is the effect of ignoring the spatial dependence of the source, since the spherical shape of the bubbles causes a suppression. In particular, in the envelope approximation the sphericity is lost at the expense of decreasing the surface area of the walls which produce the gravitational radiation.

If we replace RR' by d_b^2 in Eq. (106), we obtain a single factor of $(\tau_+^2-\tau_-^2)$ in Eq. (108). This result is plotted with a dotted black line in Fig. 9. We see that the spectrum does not change significantly, indicating that the relevant quantity which determines its shape is $\langle SS'\rangle$. In [135] we argued that it would be more realistic to relate the GW spectrum to the quantity $\langle\Delta S(t)\Delta S(t')\rangle$, with $\Delta S = S - \langle S\rangle$, rather than to $\langle S(t)S(t')\rangle$, in order to take into account the fact that the result should vanish if the surfaces at t and t' were uncorrelated. Indeed, the separation $\langle S(t)S(t')\rangle = \langle S(t)\rangle\langle S(t')\rangle$ corresponds to assuming that any two points on the bubble surface are not correlated, i.e., to approximating the probability $e^{-I_{\rm tot}} = e^{-I(t)}e^{-I(t')}e^{I_\cap(t,t',s)}$ by $e^{-I(t)}e^{-I(t')}$. Replacing S with ΔS in

[13]The additional approximation $\langle S(t)S(t')\rangle \sim \langle S(t)\rangle\langle S(t')\rangle$ simplifies significantly the expressions, but does not give the correct behavior at high frequencies. It is a smoother function of time, and therefore its Fourier transform falls more rapidly at high ω.

Eq. (106) we obtain the red lines in Fig. 9 (with and without taking into account the extra factor of RR'). Only the low-frequency part of the spectrum changes with respect to the previous approximations. The shape of the spectrum is more realistic, but it is quantitatively very similar.

VII. CONCLUSIONS AND DISCUSSION

We have studied the general features of gravitational waves from bubble collisions in the envelope approximation. For that aim we have applied the approach of Ref. [125] to this particular mechanism of GW generation. In the first place, we have computed the GW spectrum for several phase transition models. Our results for these specific models are in agreement with previous works, whereas our analytic expressions allowed us to consider wider frequency ranges as well as greater variations of parameters.

In second place, we have studied the asymptotic limits of the spectrum for arbitrary nucleation rate $\Gamma(t)$ and wall velocity $v(t)$. We have thus confirmed analytically that the GW spectrum for the envelope approximation always rises as ω^3 for low frequencies and falls as ω^{-1} for high frequencies, independently of the specific evolution of the phase transition. Therefore, in the two ends of the spectrum, it is only necessary to compute numerically the constant coefficients of these power laws. For constant velocity, the calculation of these coefficients simplifies significantly, and we obtained analytically the dependence on v. Furthermore, we provided a simple interpolation between the asymptotes, which can be used as an estimate of the whole spectrum, thus avoiding difficult numerical computations. These analytic approximations are useful for studying the dependence of the spectrum on the parameters of the model. Although in this work we have focused on the envelope approximation, we expect that our determination of the asymptotes can be generalized to other mechanisms such as the bulk flow model [123,124], where it is particularly difficult to compute the spectrum at high frequencies.

Finally, we have used our results to study the dependence of the GW spectrum on the characteristic time and distance scales of the phase transition. We have confirmed that the peak frequency ω_p is generally determined by the timescale rather than the length scale. More precisely, we have $\omega_p \sim t_b^{-1}$, where t_b is the *total duration* of the phase transition. We have checked this fact, both numerically and analytically, by varying the bubble size $d_b = vt_b$ as well as the time $t_\Gamma \leq t_b$ during which bubble nucleation is active. The amplitude of the spectrum does depend on the size scale d_b (the dimensionless spectrum Δ goes roughly as v^3). We have related these features to the time correlation of the uncollided wall surface area, which is essentially the source of GWs in the envelope approximation. Moreover, the rough approximation $\Pi \propto \langle S(t)S(t')\rangle$, which corresponds essentially to neglecting the spatial dependence of the source, gives the correct position of the peak as well as the correct behavior at low and high frequencies, although the amplitude is a few orders of magnitude too high.

Lattice simulations of vacuum bubbles generally give a different form of the spectrum. In the first place, in Ref. [119], it was found that GWs are produced after bubble percolation. However, in Ref. [120] this effect was identified with oscillations of the scalar field, which produce GWs with a frequency of the order of the scalar mass in the broken phase. Thus, with a realistic separation of scales (not achievable in the simulation), this signal will be actually at a much higher frequency, and will have a much smaller amplitude.

In Ref. [118] it was found that the GW spectrum sourced by the scalar field agrees in shape and intensity with the envelope approximation, at least in the frequency range delimited by the inverses of the box size L of the simulation and the wall width l_w. At higher frequencies the decrease becomes steeper. In the more recent simulation [120], it was found that the peak of the spectrum from bubble collisions is slightly shifted toward the infrared with respect to the envelope approximation. Besides, the power law on the high frequency side of this peak seems to be given by $b \simeq 1.5$, in contrast to the value $b = 1$ for the envelope approximation. In the subsequent work [121], the wall thickness was varied (by changing a parameter in the effective potential), and it was found that for thicker walls the ultraviolet power law has even larger values, up to $b \simeq 2.3$. The more recent work [146] supports the conclusion that the high-frequency power law becomes steeper for thick-walled bubbles.

However, we remark that the bubble radius and the wall width, which in general differ by several orders of magnitude, in the lattice simulations are separated by, at most, a couple of orders of magnitude. For instance, in [120], the power law $b \simeq 1.5$ fits the curve in a frequency range of one order of magnitude between the peak frequency ω_p and $\omega \sim 10\omega_p$. A little beyond this range is the ultraviolet bump due to the field oscillations. This second peak is associated to the scalar mass scale, which is of the same order of the wall width l_w, so this part of the curve is also influenced by this parameter. Therefore, it is possible that the differences with the envelope approximation at high frequency are due to an insufficient separation of these scales.

In order to avoid this problem, in Refs. [147,148] a two-bubble collision is first studied by lattice simulations to determine how the surface energy density scales with the bubble radius in the collided regions, and then the GW spectrum is computed in many-bubble thin-wall simulations like those of Ref. [124] for the bulk flow model. The power law exponents obtained with this approach are also different from the envelope approximation and depend on the nature of the scalar field, i.e., they are different for a real scalar field, a complex scalar field which breaks a $U(1)$

global symmetry, and the case of a gauge $U(1)$ symmetry. As already mentioned, the part of this calculation which is equivalent to the bulk flow model can be approached semianalytically, but the numerical integrals become very difficult for frequencies higher than the peak [123]. Therefore, the high-frequency approximations we used to obtain the asymptotic behavior for the envelope case will be useful to address this kind of calculation.

ACKNOWLEDGMENTS

This work was supported by CONICET Grant No. PIP 11220130100172 and Universidad Nacional de Mar del Plata, Grant No. EXA999/20. A. M. and F. A. M. are members of CONICET, Argentina.

APPENDIX A: DETAILS FOR THE SIMULTANEOUS CASE

In this Appendix we present some analytic and numerical results for the delta-function nucleation rate.

1. Gaussian integrals

The integrals

$$\tilde{Q}(\tau_+,\tau_s,\tilde{\omega}) = \int_0^{\tau_s} d\tau_- \cos(\tilde{\omega}\tau_-) Q(\tau_+,\tau_-,\tau_s) e^{-\frac{\pi}{4}\frac{(\tau_++\tau_s)^2}{\tau_s}\tau_-^2} \tag{A1}$$

and

$$\tilde{P}_i(\tau_+,\tau_s,\tilde{\omega}) = \int_0^{\tau_s} d\tau_- \cos(\tilde{\omega}\tau_-) P_i(\tau_+,\tau_-,\tau_s) e^{-\frac{\pi}{4}\frac{(\tau_++\tau_s)^2}{\tau_s}\tau_-^2}, \tag{A2}$$

where Q and P_i are the polynomials defined in Eqs. (84) and (27)–(29), are straightforward, since the polynomials are of the form $A + B\tau_-^2 + C\tau_-^4 + D\tau_-^6$ (with $D = 0$ for the P_i) and the cosine can be written as a combination of exponentials. We obtain

$$\begin{aligned}
\tilde{Q} &= (\tau_+^2 - \tau_s^2)^2[\tau_s^8 I^{(0)} - \tau_s^4(\tau_+^2 + 2\tau_s^2) I^{(2)} \\
&\quad + \tau_s^2(2\tau_+^2 + \tau_s^2) I^{(4)} - \tau_+^2 I^{(6)}], \\
\tilde{P}_0 &= (\tau_+^2 - \tau_s^2)^2(\tau_s^4 I^{(0)} - 2\tau_s^2 I^{(2)} + I^{(4)}), \\
\tilde{P}_1 &= 2(\tau_+^2 - \tau_s^2)[-(\tau_+^2 + 3\tau_s^2)\tau_s^4 I^{(0)} \\
&\quad + 2(3\tau_+^2 + \tau_s^2)\tau_s^2 I^{(2)} + (\tau_s^2 - 5\tau_+^2) I^{(4)}], \\
\tilde{P}_2 &= (3\tau_s^4 + 2\tau_+^2\tau_s^2 + 3\tau_+^4)\tau_s^4 I^{(0)} \\
&\quad + 2(\tau_s^4 + 6\tau_+^2\tau_s^2 - 15\tau_+^4)\tau_s^2 I^{(2)} \\
&\quad + (3\tau_s^4 - 30\tau_+^2\tau_s^2 + 35\tau_+^4) I^{(4)}.
\end{aligned} \tag{A3}$$

where the quantities $I^{(n)}$ are the integrals

$$\begin{aligned}
I^{(n)} &= \int_0^{\tau_s} d\tau_- \tau_-^n \cos(\tilde{\omega}\tau_-) e^{-\alpha\tau_-^2} \\
&= \mathrm{Re}\left[\int_0^{\tau_s} d\tau_- \tau_-^n e^{-\alpha\tau_-^2 - i\tilde{\omega}\tau_-}\right],
\end{aligned} \tag{A4}$$

with $\alpha = \frac{\pi}{4}(\tau_+ + \tau_s)^2/\tau_s$. These are given by

$$I^{(0)} = \sqrt{\frac{\pi}{4\alpha}} \exp\left(-\frac{\tilde{\omega}^2}{4\alpha}\right) \mathrm{Re}\left[\mathrm{erf}\left(\sqrt{\alpha}\tau_s + \frac{i\tilde{\omega}}{2\sqrt{\alpha}}\right)\right], \tag{A5}$$

$$I^{(2)} = \frac{1}{4\alpha^2}[(2\alpha - \tilde{\omega}^2) I^{(0)} + S - C], \tag{A6}$$

$$\begin{aligned}
I^{(4)} &= \frac{1}{16\alpha^4}[(\tilde{\omega}^4 - 12\alpha\tilde{\omega}^2 + 12\alpha^2) I^{(0)} \\
&\quad - (\tilde{\omega}^2 - 4\alpha^2\tau_s^2 - 10\alpha) S + (\tilde{\omega}^2 - 4\alpha^2\tau_s^2 - 6\alpha) C],
\end{aligned} \tag{A7}$$

$$\begin{aligned}
I^{(6)} &= \frac{1}{64\alpha^6}[(-\tilde{\omega}^6 + 30\alpha\tilde{\omega}^4 - 180\alpha^2\tilde{\omega}^2 + 120\alpha^3) I^{(0)} \\
&\quad + (\tilde{\omega}^4 - 4\alpha^2\tau_s^2\tilde{\omega}^2 - 28\alpha\tilde{\omega}^2 + 16\alpha^4\tau_s^4 + 72\alpha^3\tau_s^2 + 132\alpha^2) S \\
&\quad - (\tilde{\omega}^4 - 4\alpha^2\tau_s^2\tilde{\omega}^2 - 24\alpha\tilde{\omega}^2 + 16\alpha^4\tau_s^4 + 40\alpha^3\tau_s^2 + 60\alpha^2) C],
\end{aligned} \tag{A8}$$

where

$$S = e^{-\alpha\tau_s^2}\tilde{\omega}\sin(\tilde{\omega}\tau_s), \qquad C = 2\alpha\tau_s e^{-\alpha\tau_s^2}\cos(\tilde{\omega}\tau_s), \tag{A9}$$

and $\mathrm{Re}[\mathrm{erf}(z)]$ is the real part of the error function.

On the other hand, for the approximation (108), we have to calculate the integral

$$\tilde{P} = \int_0^{\tau_s} d\tau_- \cos(\tilde{\omega}\tau_-)(\tau_+^2 - \tau_-^2)^2 e^{-\frac{\pi}{4}\frac{(\tau_++\tau_s)^2}{\tau_s}\tau_-^2}. \tag{A10}$$

which has the same form of Eq. (A2), but for the function $P = \tau_+^4 - 2\tau_+^2\tau_-^2 + \tau_-^4$ instead of P_i. We obtain in this case $\tilde{P} = \tau_+^4 I^{(0)} - 2\tau_+^2 I^{(2)} + I^{(4)}$, and Eq. (108) is given by

$$\Delta \sim v^3\tilde{\omega}^3 \int_0^{\infty} d\tau_+ \int_0^{\tau_+} d\tau_s \tau_s \tilde{P} e^{-\frac{\pi}{12}(2\tau_+^3 - \tau_s^3 + 3\tau_+^2\tau_s)}. \tag{A11}$$

If RR' is replaced by d_b^2 in Eq. (106), then we have a single factor of $(\tau_+^2 - \tau_-^2)$ in Eq. (108), so we have to calculate the integral (A10) with $P = \tau_+^2 - \tau_-^2$, and we obtain in this case $\tilde{P} = \tau_+^2 I^{(0)} - I^{(2)}$. If $\langle \Delta S(t)\Delta S(t')\rangle$ is used instead of $\langle S(t)S(t')\rangle$ in Eq. (106), then, in the integrand of Eq. (A11), we have to subtract, to the quantity $\tilde{P}e^{-I_{\mathrm{tot}}}$, the same quantity evaluated at $\tau_s = \tau_+$.

2. Contributions to the spectrum

It is of interest to show separately the single-bubble and the two-bubble contributions. In Fig. 10 we consider the case of simultaneous nucleation for a few velocities (the exponential case was already considered in Ref. [122]).

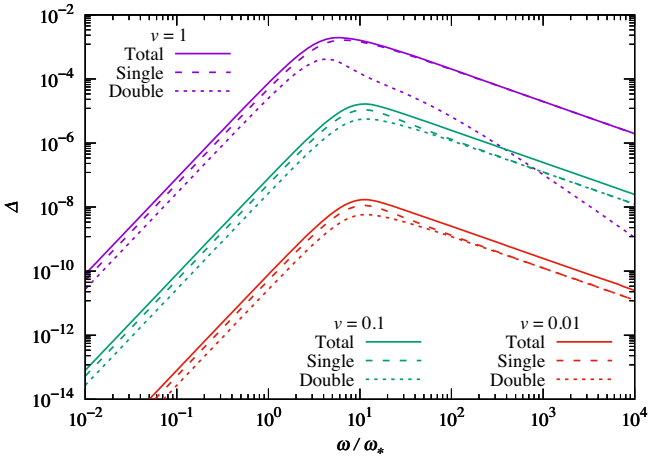

FIG. 10. The different contributions to the spectrum for the case of simultaneous nucleation, for a few values of the wall velocity v ($\omega_* = v/d_b$).

We see that the two contributions are in general of the same order, except for the case $v = 1$, where the intensity falls as ω^{-2} for $\omega/\omega_b \gg 1$, as shown analytically in Sec. III.

APPENDIX B: DETAILS FOR THE GAUSSIAN CASE

In Sec. V C we have considered as a reference time the parameter $t_{\rm min}$ and as a reference frequency $\omega_* = t_{\rm min}^{-1}$. Thus, in Eqs. (71)–(74), we have $\tilde{\omega} \equiv \omega/\omega_* = \omega t_{\rm min}$, and the dimensionless times are given by Eq. (54) with $t_* = t_m$ and $t_b = t_{\rm min}$. For instance, we have $\tau = (t - t_m)/t_{\rm min}$. The dimensionless rate is given by $\tilde{\Gamma}(\tau) = (\alpha/\sqrt{\pi})e^{-(\alpha\tau)^2}$, and the integrals in Eqs. (72) and (74) can be done analytically, as well as those in Eqs. (2) and (22). To simplify a little the expressions, in this Appendix we shall consider the parameter t_Γ as the reference time, and the corresponding reference frequency $\omega_* = t_\Gamma^{-1} = \gamma$. To avoid confusion, we shall denote the dimensionless spectrum (18) as $\bar{\Delta}$, and we shall denote $\bar{\omega} \equiv \omega/\omega_* = \omega t_\Gamma$. The relation with $\tilde{\omega}$ and the corresponding spectrum is $\bar{\omega} = \tilde{\omega}/\alpha$, $\bar{\Delta}(\bar{\omega}) = \alpha^2\Delta(\alpha\bar{\omega})$. We also denote the corresponding dimensionless times by $x = (t - t_m)/t_\Gamma$, $x_N = (t_N - t_m)/t_\Gamma$, etc., which corresponds to the change of variables $x = \alpha\tau$, $x_N = \alpha\tau_N$, etc. in Eqs. (71)–(74).

1. Formulas for the spectrum and the asymptotes

We obtain

$$\bar{\Delta}^{(s)} = \frac{v^3\bar{\omega}^3}{48\alpha^3}\int_{-\infty}^{\infty} dx_+ \int_0^{\infty} dx_- \cos(\bar{\omega}x_-) \int_{x_-}^{\infty} \frac{dx_s}{x_s^3} \sum_{i=0}^{2} \frac{j_i(v\bar{\omega}x_s)}{(v\bar{\omega}x_s)^i} F_i e^{-I_{\rm tot}}. \tag{B1}$$

$$\bar{\Delta}^{(d)} = \frac{\pi v^3\bar{\omega}^3}{48\alpha^6}\int_{-\infty}^{\infty} dx_+ \int_0^{\infty} dx_- \cos(\bar{\omega}x_-) \int_{x_-}^{\infty} \frac{dx_s}{x_s^4} \frac{j_2(v\bar{\omega}x_s)}{(v\bar{\omega}x_s)^2} G_+ G_- e^{-I_{\rm tot}}, \tag{B2}$$

where the functions F_i, $G_\pm$, and $I_{\rm tot}$ are given by

$$F_0 = \frac{(x_-^2 - x_s^2)^2}{2}\left\{(x_s^4 + x_+^4 - 4x_s^2 - 2x_+^2x_s^2 + 12x_+^2 + 12)\left[\mathrm{erf}\left(\frac{x_+ - x_s}{2}\right) + 1\right] + (x_+^3 - x_s^3 + x_+^2x_s - x_+x_s^2 + 10x_+ + 6x_s)\frac{2}{\sqrt{\pi}}e^{-\frac{1}{4}(x_+ - x_s)^2}\right\}, \tag{B3}$$

$$\begin{aligned} F_1 = (x_s^2 - x_-^2)\Big\{&(3x_s^6 + x_-^2x_s^4 - 2x_+^2x_s^4 - x_+^4x_s^2 + 5x_-^2x_+^4 - 6x_-^2x_+^2x_s^2 \\ &- 4x_s^4 - 12x_-^2x_s^2 - 12x_+^2x_s^2 + 60x_-^2x_+^2 - 12x_s^2 + 60x_-^2)\left[\mathrm{erf}\left(\frac{x_+ - x_s}{2}\right) + 1\right] \\ &- (3x_s^5 + 3x_+x_s^4 + x_-^2x_s^3 + x_+^2x_s^3 - 5x_-^2x_+^2x_s - 5x_-^2x_+^3 + x_+^3x_s^2 + x_-^2x_+x_s^2 \\ &+ 6x_s^3 + 10x_+x_s^2 - 30x_-^2x_s - 50x_-^2x_+)\frac{2}{\sqrt{\pi}}e^{-\frac{1}{4}(x_+ - x_s)^2}\Big\}, \end{aligned} \tag{B4}$$

$$
\begin{aligned}
F_2 = {} & (3x_s^8 + 2x_-^2 x_s^6 + 2x_+^2 x_s^6 + 4x_s^6 + 3x_-^4 x_s^4 + 3x_+^4 x_s^4 + 24x_-^2 x_s^4 + 12x_-^2 x_+^2 x_s^4 + 36x_+^2 x_s^4 \\
& + 36x_s^4 - 60x_-^4 x_s^2 - 30x_-^2 x_+^4 x_s^2 - 360x_-^2 x_s^2 - 30x_-^4 x_+^2 x_s^2 - 360x_-^2 x_+^2 x_s^2 + 420x_-^4 \\
& + 35x_-^4 x_+^4 + 420x_-^4 x_+^2)\frac{1}{2}\left[\operatorname{erf}\left(\frac{x_+ - x_s}{2}\right) + 1\right] \\
& + (5x_s^7 + 5x_+ x_s^6 - 18x_-^2 x_s^5 + 3x_+^2 x_s^5 + 18x_s^5 + 3x_+^3 x_s^4 - 18x_-^2 x_+ x_s^4 + 30x_+ x_s^4 + 5x_-^4 x_s^3 \\
& - 180x_-^2 x_s^3 - 30x_-^2 x_+^2 x_s^3 - 30x_-^2 x_+^3 x_s^2 + 5x_-^4 x_+ x_s^2 - 300x_-^2 x_+ x_s^2 + 210x_-^4 x_s \\
& + 35x_-^4 x_+^2 x_s + 35x_-^4 x_+^3 + 350x_-^4 x_+)\frac{1}{\sqrt{\pi}} e^{-\frac{1}{4}(x_+ - x_s)^2},
\end{aligned} \tag{B5}
$$

$$
\begin{aligned}
G_\pm = {} & \frac{(x_-^2 - x_s^2)}{2}\left\{[x_s^4 - x_+^2 x_s^2 - 2x_s^2 \pm x_-(x_+^3 + 6x_+ - x_+ x_s^2)]\left[\operatorname{erf}\left(\frac{x_+ - x_s}{2}\right) + 1\right]\right. \\
& \left. -2[x_s^3 + x_+ x_s^2 \mp x_-(x_+ x_s + x_+^2 + 4)]\frac{1}{\sqrt{\pi}} e^{-\frac{1}{4}(x_+ - x_s)^2}\right\},
\end{aligned} \tag{B6}
$$

and $I_{\mathrm{tot}} = I((x_+ - x_-)/2, \alpha) + I((x_+ + x_-)/2, \alpha) + I_\cap$, with

$$
I(x, \alpha) = \frac{\pi}{3\alpha^3}\left\{x(2x^2 + 3)[\operatorname{erf}(x) + 1] + (x^2 + 1)\frac{2}{\sqrt{\pi}} e^{-x^2}\right\} \tag{B7}
$$

and

$$
\begin{aligned}
I_\cap = {} & \frac{\pi\alpha^{-3}}{24x_s}\left\{(3x_-^2 x_s + 2x_+^2 x_s - x_s^3 - x_+ x_s^2 + 8x_s - 3x_-^2 x_+)\frac{2}{\sqrt{\pi}} e^{-\frac{1}{4}(x_+ - x_s)^2}\right. \\
& \left. + (x_s^4 - 3x_-^2 x_s^2 - 3x_+^2 x_s^2 - 6x_s^2 + 2x_+^3 x_s + 6x_-^2 x_+ x_s + 12x_+ x_s - 6x_-^2 - 3x_-^2 x_+^2)\left[\operatorname{erf}\left(\frac{x_+ - x_s}{2}\right) + 1\right]\right\}.
\end{aligned} \tag{B8}
$$

The coefficient of the low-frequency asymptote (62) is given by ($\bar{D} = \alpha^5 D$)

$$
\bar{D} = \frac{\alpha^{-3}}{48}\int_{-\infty}^{\infty} dx_+ \int_0^{\infty} dx_- \int_{x_-}^{\infty} \frac{dx_s}{x_s^3}\left[F_0 + \frac{F_1}{3} + \frac{F_2}{15} + \frac{\pi G_+ G_-}{15\alpha^3 x_s}\right] e^{-I_{\mathrm{tot}}}. \tag{B9}
$$

The coefficients of the high-frequency asymptote (64)–(65) are given by ($\bar{C}^{(s)} = \alpha C^{(s)}$)

$$
\bar{C}^{(s)} = \frac{\pi}{72}\int_{-\infty}^{\infty} d\bar{x} e^{-\frac{4\pi}{3}\tilde{I}_3(\bar{x})}\tilde{I}_4(\bar{x})\tilde{I}_2(\bar{x}), \qquad \bar{C}^{(d)} = \frac{\pi}{18}\int_{-\infty}^{\infty} d\bar{x} e^{-\frac{4\pi}{3}\tilde{I}_3(\bar{x})}\tilde{I}_3(\bar{x})^2, \tag{B10}
$$

with

$$
\tilde{I}_2 = \alpha^{-2}\left\{\frac{2\bar{x}^2 + 1}{4}[\operatorname{erf}(\bar{x}) + 1] + \frac{\bar{x}}{2\sqrt{\pi}} e^{-\bar{x}^2}\right\}, \tag{B11}
$$

$$
\tilde{I}_3 = \alpha^{-3}\left\{\frac{\bar{x}(2\bar{x}^2 + 3)}{4}[\operatorname{erf}(\bar{x}) + 1] + \frac{\bar{x}^2 + 1}{2\sqrt{\pi}} e^{-\bar{x}^2}\right\}, \tag{B12}
$$

$$
\tilde{I}_4 = \alpha^{-4}\left\{\frac{4\bar{x}^4 + 12\bar{x}^2 + 3}{8}[\operatorname{erf}(\bar{x}) + 1] + \frac{\bar{x}(2\bar{x}^2 + 5)}{4\sqrt{\pi}} e^{-\bar{x}^2}\right\}. \tag{B13}
$$

2. Different parametrizations

The parametrization (10) for the nucleation rate,

$$\Gamma(t) = \Gamma_m e^{-\gamma^2(t-t_m)^2}, \tag{B14}$$

is centered at the maximum of the Gaussian. We have conveniently defined the time parameters $t_\Gamma = \gamma^{-1}$ and $t_{\min} = d_{\min}/v = v^{-1}(\gamma/\sqrt{\pi}\Gamma_m)^{1/3}$ in order to obtain the simple expression (13) where the dimensionless rate $\tilde{\Gamma}$ depends only on the parameter $\alpha = t_{\min}/t_\Gamma$. In terms of the basic parameters of the Gaussian, we have

$$\alpha^3 = \frac{\gamma^4}{\sqrt{\pi} v^3 \Gamma_m}. \tag{B15}$$

In Fig. 11 we consider the evolution of the phase transition for different values of α. We see that, for $\alpha \gtrsim 1$, the development of the phase transition takes place around the time t_m or later. Hence, in these cases the number density of nucleated bubbles is maximal (i.e., it is given by the integral of the Gaussian), and we have $d_b \simeq d_{\min} = n_{\max}^{-1/3}$ and the duration of the phase transition is given by $t_b \simeq t_{\min}$. Besides, we see that the parameter t_Γ gives an estimate of the duration of bubble nucleation. In the limit $\alpha \to \infty$, the time t_Γ becomes infinitely smaller than t_b, and the nucleation rate becomes a delta function.

In contrast, for small α (left panel in Fig. 11) the phase transition is completed before $t = t_m$, and neither $t_{\min}$ nor t_Γ give a correct estimate for its duration. The limit $\alpha \to 0$ corresponds either to $\gamma \to 0$ or to $\Gamma_m \to \infty$. Since the phase transition takes place away from the maximum of the Gaussian, we expect that the usual exponential approximation should be valid in this limit. To investigate this, we notice that, for any t_*, we may write $t - t_m = t - t_* + t_* - t_m$ in Eq. (B14), and we obtain

$$\Gamma(t) = \Gamma_* e^{\beta(t-t_*)-\gamma^2(t-t_*)^2}, \tag{B16}$$

where

$$\Gamma_* = \Gamma_m e^{-\gamma^2(t_m-t_*)^2}, \qquad \beta = 2\gamma^2(t_m - t_*) \tag{B17}$$

(notice that β depends on the time t_*). Let us consider the time t_e at which $I = 1$ ($f_+ = e^{-1}$). The corresponding dimensionless variable $x_e = (t_e - t_m)/t_\Gamma$ is given by the equation $I(x_e, 1) = \alpha^3$, where $I(x, \alpha)$ is given by Eq. (B7). For $t_* = t_e$ we have $\beta = 2\gamma|x_e|$ and $\Gamma_* = \Gamma_m e^{-x_e^2}$. The function $I(x, 1)$ grows monotonically from $I(-\infty, 1) = 0$. This can be seen more clearly from the definition of $I(t)$, Eq. (2). Hence, for $\alpha \to 0$ we have $x_e \to -\infty$. This implies, in the first place, that $t_e - t_m \to -\infty$, and, in the second place, that $\gamma/\beta \propto |x_e|^{-1} \to 0$, so Eq. (B16) becomes indeed an exponential rate in this limit. For large and negative x we have $I(x, 1) \simeq \sqrt{\pi} e^{-x^2}/2x^4$, so the equation for x_e becomes $\sqrt{\pi} e^{-x_e^2}/2x_e^4 \simeq \alpha^3$, and using the relation (B15), we obtain $\Gamma_* \simeq 2\gamma^4 x_e^4/\pi v^3 = \beta^4/8\pi v^3$. Hence, in this limit Eq. (B16) coincides with our parametrization (9),

$$\Gamma(t) = \frac{\beta^4}{8\pi v^3} e^{\beta(t-t_e)}. \tag{B18}$$

In Ref. [126], the GW spectrum was calculated for a nucleation rate of the form

$$\Gamma(t) = H_*^4 e^{\beta(t-t_*)-\gamma^2(t-t_*)^2}. \tag{B19}$$

As we discussed in Sec. II, this model is motivated by an expansion of the instanton action S in powers of $t - t_*$. For many physical models we have $\gamma \ll \beta$. Indeed, the usual approximation is to neglect γ, which leads to the exponential nucleation rate. Notice that, in this parametrization, t_* is the time at which $\Gamma = H_*^4$, while the phase transition takes place at a later time, which is roughly given by $\Gamma \sim \beta^4$ (in general, β is a few orders of magnitude higher than H_*). Therefore, a new parametrization is used in [126],

$$\Gamma(t) = \beta'^4 e^{\beta'(t-t'_*)-\gamma^2(t-t'_*)^2}. \tag{B20}$$

Here, t'_* is the time at which $\Gamma = \beta'^4$, and for $\gamma = 0$ we have $\beta' = \beta$. On the other hand, for $\gamma \neq 0$ the nucleation rate (B20) is a Gaussian and can be written in the form (B14). The parametrizations (B20) and (B14) are related by [126]

$$\Gamma_m = \beta'^4 e^{\beta'^2/4\gamma^2}, \qquad t'_* = t_m - \beta'/2\gamma^2. \tag{B21}$$

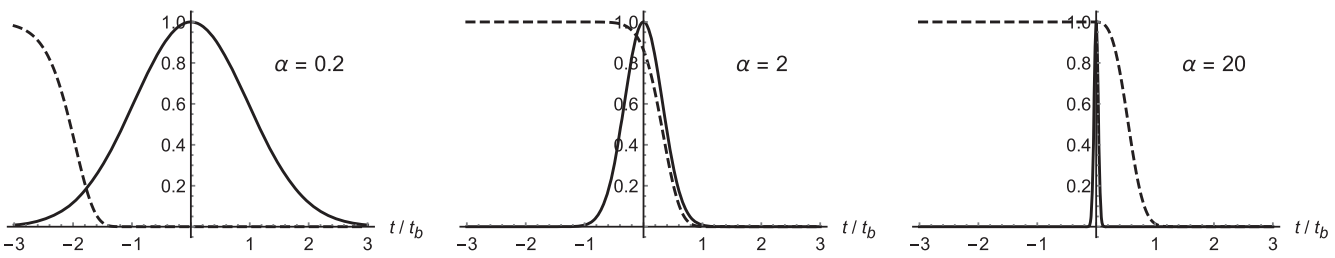

FIG. 11. The nucleation rate Γ/Γ_m (solid lines) and the fraction of volume remaining in the high-temperature phase f_+ (dashed lines) for $v = 1$.

The results of Ref. [126] depend on the ratio γ/β' and the velocity v. The relation with our dimensionless parameter $\alpha = \gamma t_b$ is

$$\sqrt{\pi} v^3 (\gamma t_b)^3 = (\gamma/\beta')^4 e^{-(\beta'/\gamma)^2/4}. \tag{B22}$$

We remark that, for $\gamma \ll \beta$, the phase transition completes in a time of order β^{-1} well before the time t_m is reached. Therefore, in the relevant time interval we may expand the exponential $e^{-\gamma^2(t-t_*)^2}$ and obtain a perturbative expansion in powers of γ/β, where each term of the expansion is computed using the exponential rate. Thus, we obtain the lowest correction to the exponential case by writing Eq. (B16) as

$$\Gamma(t) = \Gamma_* e^{\beta(t-t_*)}[1 - \gamma^2 (t - t_*)^2]. \tag{B23}$$

Taking $t_* = t_e$, where now t_e is the time corresponding to $f_+ = 1$ for the exponential rate, the first factors in (B23) are of the form (B18). The dimensionless nucleation rate is in this case

$$\tilde{\Gamma}(\tau) = (e^\tau/8\pi)[1 - (\gamma/\beta)^2 \tau^2] \tag{B24}$$

(with $\tau = \beta t$). Hence, the correction to the exponential case is given by Eqs. (71)–(74), with the polynomials P_i replaced by $-(\gamma/\beta)^2 \tau_N^2 P_i$ in Eq. (72), and the same for $Q_\pm$ in Eq. (74). The integrals in these equations can be done analytically, and the functions F_i and $G_\pm$ are of the form (75), where $\tilde{F}_i$ and $\tilde{G}$ are polynomials which are now more cumbersome than Eqs. (76)–(79). In any case, computing this correction to the exponential case may be more useful than considering a Gaussian rate. We shall investigate this kind of approximation elsewhere.

In the opposite case, in which the phase transition occurs around the time t_m, the parametrization (B20) in terms of β' is no longer useful. In particular, according to Eqs. (B21), we have $t'_* \to t_m$ only for $\beta' \to 0$ or $\gamma \to \infty$. In practice, we may have $\beta' > \gamma$ and the bubble nucleation still occur in a time γ^{-1} around t_m, while the reference time t'_* may fall outside the relevant range. Therefore, if the value of γ is calculated by expanding S around the corresponding temperature T'_*, the error may be large. Let us consider some specific examples from physically motivated models. In the case of strong supercooling considered in Ref. [90] we have typical values $\gamma/H_* \sim 10, \Gamma_m/H_*^4 \sim 1000$. This gives, according to Eq. (B21), a ratio β'/γ in the range 2–3 and $t_m - t'_* \simeq \gamma^{-1}$. On the other hand, in the case of reheating, for the physical model considered in Ref. [134] we have $\Gamma_m/H_*^4 \sim 10^{17}$–$10^{18}$ and $\gamma/H_* \sim 10^3$–10^4. This gives $\beta'/\gamma \simeq$ 9–10 and $t_m - t'_* \simeq 5\gamma^{-1}$.

APPENDIX C: THE SHAPE OF THE SPECTRUM

The GW spectrum for both the exponential nucleation and the simultaneous nucleation were computed in Ref. [118] for $v = 1$, and Fig. 3 of that work can be directly compared with our solid and dashed curves for $v = 1$ in Fig. 6. The results are in qualitative agreement for the shapes of the curves as well as for the relative positions of the peak for the two models. Quantitatively, though, our results have order 1 differences with those simulations. Nevertheless, for the exponential case, our results are in agreement with more recent simulations [124] as well as with the semianalytic treatment of Ref. [122].

The numerical results of Ref. [126] for the Gaussian case were presented with the frequency and amplitude of the GW spectrum Δ normalized with their peak values ω_p, Δ_p. In this way, the maximum of the spectra for different model parameters coincide. The information on the values of ω_p and Δ_p is lost, but the shape of the spectra can be directly compared. We consider a similar plot in Fig. 12 for the two limiting cases of the Gaussian nucleation rate, namely, $\alpha \to 0$ (exponential rate) and $\alpha \to \infty$ (delta-function rate). The curves for different values of α fall between these two cases. Only the range $0.1 \lesssim \omega/\omega_p \lesssim 3$ was considered in Ref. [126], due to numerical difficulties of their multidimensional integration. The inset in Fig. 12 shows this range for a better comparison. It can be appreciated that these curves are in agreement with those of [126].

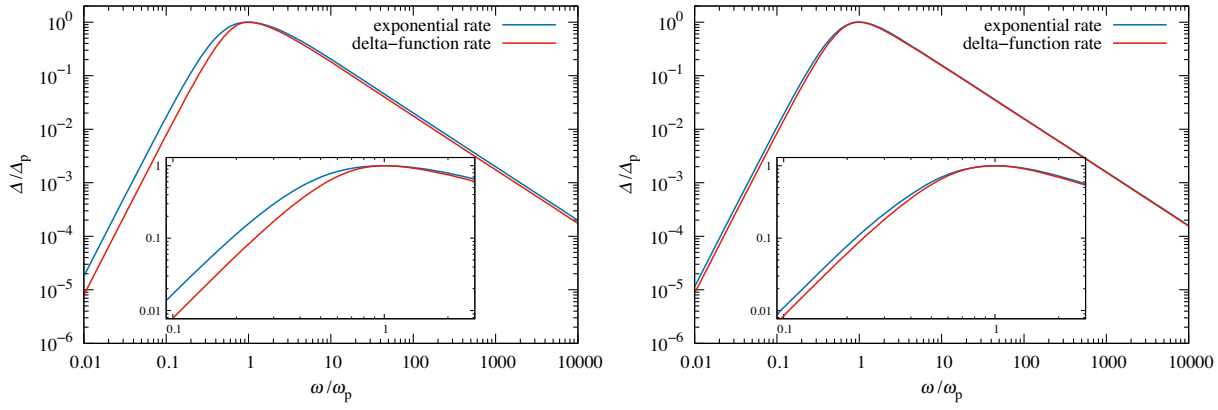

FIG. 12. The spectral shape for the exponential and the delta-function rates, for $v = 1$ (left) and $v = 0.3$ (right).

[1] V. Kuzmin, V. Rubakov, and M. Shaposhnikov, On the anomalous electroweak baryon number nonconservation in the early universe, Phys. Lett. **155B**, 36 (1985).
[2] A. G. Cohen, D. Kaplan, and A. Nelson, Progress in electroweak baryogenesis, Annu. Rev. Nucl. Part. Sci. **43**, 27 (1993).
[3] M. S. Turner and F. Wilczek, Relic Gravitational Waves and Extended Inflation, Phys. Rev. Lett. **65**, 3080 (1990).
[4] LISA Collaboration, Laser interferometer space antenna, arXiv:1702.00786.
[5] R. Apreda, M. Maggiore, A. Nicolis, and A. Riotto, Gravitational waves from electroweak phase transitions, Nucl. Phys. **B631**, 342 (2002).
[6] A. Megevand, Gravitational waves from deflagration bubbles in first-order phase transitions, Phys. Rev. D **78**, 084003 (2008).
[7] J. R. Espinosa, T. Konstandin, J. M. No, and M. Quiros, Some cosmological implications of hidden sectors, Phys. Rev. D **78**, 123528 (2008).
[8] S. J. Huber and T. Konstandin, Production of gravitational waves in the nMSSM, J. Cosmol. Astropart. Phys. 05 (2008) 017.
[9] A. Ashoorioon and T. Konstandin, Strong electroweak phase transitions without collider traces, J. High Energy Phys. 07 (2009) 086.
[10] L. Leitao, A. Megevand, and A. D. Sanchez, Gravitational waves from the electroweak phase transition, J. Cosmol. Astropart. Phys. 10 (2012) 024.
[11] G. C. Dorsch, S. J. Huber, and J. M. No, Cosmological Signatures of a UV-Conformal Standard Model, Phys. Rev. Lett. **113**, 121801 (2014).
[12] M. Kakizaki, S. Kanemura, and T. Matsui, Gravitational waves as a probe of extended scalar sectors with the first order electroweak phase transition, Phys. Rev. D **92**, 115007 (2015).
[13] K. Hashino, M. Kakizaki, S. Kanemura, and T. Matsui, Synergy between measurements of gravitational waves and the triple-Higgs coupling in probing the first-order electroweak phase transition, Phys. Rev. D **94**, 015005 (2016).
[14] M. Chala, G. Nardini, and I. Sobolev, Unified explanation for dark matter and electroweak baryogenesis with direct detection and gravitational wave signatures, Phys. Rev. D **94**, 055006 (2016).
[15] S. J. Huber, T. Konstandin, G. Nardini, and I. Rues, Detectable gravitational waves from very strong phase transitions in the general NMSSM, J. Cosmol. Astropart. Phys. 03 (2016) 036.
[16] L. Leitao and A. Megevand, Gravitational waves from a very strong electroweak phase transition, J. Cosmol. Astropart. Phys. 05 (2016) 037.
[17] F. P. Huang, Y. Wan, D.-G. Wang, Y.-F. Cai, and X. Zhang, Hearing the echoes of electroweak baryogenesis with gravitational wave detectors, Phys. Rev. D **94**, 041702 (2016).
[18] M. Garcia-Pepin and M. Quiros, Strong electroweak phase transition from Supersymmetric Custodial Triplets, J. High Energy Phys. 05 (2016) 177.
[19] J. Kubo and M. Yamada, Scale genesis and gravitational wave in a classically scale invariant extension of the standard model, J. Cosmol. Astropart. Phys. 12 (2016) 001.
[20] P. Huang, A. J. Long, and L.-T. Wang, Probing the electroweak phase transition with Higgs factories and gravitational waves, Phys. Rev. D **94**, 075008 (2016).
[21] K. Hashino, M. Kakizaki, S. Kanemura, P. Ko, and T. Matsui, Gravitational waves and Higgs boson couplings for exploring first order phase transition in the model with a singlet scalar field, Phys. Lett. B **766**, 49 (2017).
[22] M. Artymowski, M. Lewicki, and J. D. Wells, Gravitational wave and collider implications of electroweak baryogenesis aided by non-standard cosmology, J. High Energy Phys. 03 (2017) 066.
[23] V. Vaskonen, Electroweak baryogenesis and gravitational waves from a real scalar singlet, Phys. Rev. D **95**, 123515 (2017).
[24] G. C. Dorsch, S. J. Huber, T. Konstandin, and J. M. No, A second Higgs doublet in the early universe: Baryogenesis and gravitational waves, J. Cosmol. Astropart. Phys. 05 (2017) 052.
[25] A. Beniwal, M. Lewicki, J. D. Wells, M. White, and A. G. Williams, Gravitational wave, collider and dark matter signals from a scalar singlet electroweak baryogenesis, J. High Energy Phys. 08 (**2017**) 108.
[26] L. Marzola, A. Racioppi, and V. Vaskonen, Phase transition and gravitational wave phenomenology of scalar conformal extensions of the Standard Model, Eur. Phys. J. C **77**, 484 (2017).
[27] R.-G. Cai, M. Sasaki, and S.-J. Wang, The gravitational waves from the first-order phase transition with a dimension-six operator, J. Cosmol. Astropart. Phys. 08 (2017) 004.
[28] A. Kobakhidze, C. Lagger, A. Manning, and J. Yue, Gravitational waves from a supercooled electroweak phase transition and their detection with pulsar timing arrays, Eur. Phys. J. C **77**, 570 (2017).
[29] Z. Kang, P. Ko, and T. Matsui, Strong first order EWPT and strong gravitational waves in Z_3-symmetric singlet scalar extension, J. High Energy Phys. 02 (2018) 115.
[30] E. Megías, G. Nardini, and M. Quirós, Cosmological phase transitions in warped space: Gravitational waves and collider signatures, J. High Energy Phys. 09 (2018) 095.
[31] A. Alves, T. Ghosh, H.-K. Guo, K. Sinha, and D. Vagie, Collider and gravitational wave complementarity in exploring the singlet extension of the standard model, J. High Energy Phys. 04 (2019) 052.
[32] M. Chala, M. Ramos, and M. Spannowsky, Gravitational wave and collider probes of a triplet Higgs sector with a low cutoff, Eur. Phys. J. C **79**, 156 (2019).
[33] K. Miura, H. Ohki, S. Otani, and K. Yamawaki, Gravitational waves from walking technicolor, J. High Energy Phys. 10 (2019) 194.
[34] T. Prokopec, J. Rezacek, and B. Świeżewska, Gravitational waves from conformal symmetry breaking, J. Cosmol. Astropart. Phys. 02 (2019) 009.
[35] C. Marzo, L. Marzola, and V. Vaskonen, Phase transition and vacuum stability in the classically conformal B–L model, Eur. Phys. J. C **79**, 601 (2019).
[36] A. Addazi, A. Marcianò, A. P. Morais, R. Pasechnik, R. Srivastava, and J. W. F. Valle, Gravitational footprints of

massive neutrinos and lepton number breaking, Phys. Lett. B **807**, 135577 (2020).
[37] A. P. Morais and R. Pasechnik, Probing multi-step electroweak phase transition with multi-peaked primordial gravitational waves spectra, J. Cosmol. Astropart. Phys. 04 (2020) 036.
[38] A. Eichhorn, J. Lumma, J. M. Pawlowski, M. Reichert, and M. Yamada, Universal gravitational-wave signatures from heavy new physics in the electroweak sector, J. Cosmol. Astropart. Phys. 05 (2021) 006.
[39] D. Borah, A. Dasgupta, K. Fujikura, S. K. Kang, and D. Mahanta, Observable gravitational waves in minimal scotogenic model, J. Cosmol. Astropart. Phys. 08 (2020) 046.
[40] C. Grojean and G. Servant, Gravitational waves from phase transitions at the electroweak scale and beyond, Phys. Rev. D **75**, 043507 (2007).
[41] P. Schwaller, Gravitational Waves from a Dark Phase Transition, Phys. Rev. Lett. **115**, 181101 (2015).
[42] P. S. B. Dev and A. Mazumdar, Probing the scale of new physics by advanced LIGO/VIRGO, Phys. Rev. D **93**, 104001 (2016).
[43] J. Jaeckel, V. V. Khoze, and M. Spannowsky, Hearing the signal of dark sectors with gravitational wave detectors, Phys. Rev. D **94**, 103519 (2016).
[44] R. Jinno and M. Takimoto, Probing a classically conformal B-L model with gravitational waves, Phys. Rev. D **95**, 015020 (2017).
[45] C. Balazs, A. Fowlie, A. Mazumdar, and G. White, Gravitational waves at aLIGO and vacuum stability with a scalar singlet extension of the Standard Model, Phys. Rev. D **95**, 043505 (2017).
[46] I. Baldes, Gravitational waves from the asymmetric-dark-matter generating phase transition, J. Cosmol. Astropart. Phys. 05 (2017) 028.
[47] K. Tsumura, M. Yamada, and Y. Yamaguchi, Gravitational wave from dark sector with dark pion, J. Cosmol. Astropart. Phys. 07 (2017) 044.
[48] D. Croon, V. Sanz, and G. White, Model discrimination in gravitational wave spectra from dark phase transitions, J. High Energy Phys. 08 (**2018**) 203.
[49] K. Hashino, R. Jinno, M. Kakizaki, S. Kanemura, T. Takahashi, and M. Takimoto, Selecting models of first-order phase transitions using the synergy between collider and gravitational-wave experiments, Phys. Rev. D **99**, 075011 (2019).
[50] E. Madge and P. Schwaller, Leptophilic dark matter from gauged lepton number: Phenomenology and gravitational wave signatures, J. High Energy Phys. 02 (2019) 048.
[51] D. Croon, T. E. Gonzalo, and G. White, Gravitational waves from a Pati-Salam phase transition, J. High Energy Phys. 02 (2019) 083.
[52] I. Baldes and C. Garcia-Cely, Strong gravitational radiation from a simple dark matter model, J. High Energy Phys. 05 (2019) 190.
[53] V. Brdar, A. J. Helmboldt, and J. Kubo, Gravitational waves from first-order phase transitions: LIGO as a window to unexplored seesaw scales, J. Cosmol. Astropart. Phys. 02 (2019) 021.
[54] M. Fairbairn, E. Hardy, and A. Wickens, Hearing without seeing: Gravitational waves from hot and cold hidden sectors, J. High Energy Phys. 07 (2019) 044.
[55] M. Ahmadvand, K. B. Fadafan, and S. Rezapour, Gravitational waves of a first-order QCD phase transition at finite coupling from holography, arXiv:2006.04265.
[56] J. Ellis, M. Lewicki, and J. M. No, Gravitational waves from first-order cosmological phase transitions: Lifetime of the sound wave source, J. Cosmol. Astropart. Phys. 07 (2020) 050.
[57] A. Azatov, D. Barducci, and F. Sgarlata, Gravitational traces of broken gauge symmetries, J. Cosmol. Astropart. Phys. 07 (2020) 027.
[58] B. Fornal, Gravitational wave signatures of lepton universality violation, Phys. Rev. D **103**, 015018 (2021).
[59] D. Blas and A. C. Jenkins, Bridging the μHz Gap in the Gravitational-wave Landscape with Binary Resonance, arXiv:2107.04601 [Phys. Rev. Lett. (to be published)].
[60] B.-H. Liu, L. D. McLerran, and N. Turok, Bubble nucleation and growth at a baryon number producing electroweak phase transition, Phys. Rev. D **46**, 2668 (1992).
[61] N. Turok, Electroweak Bubbles: Nucleation and Growth, Phys. Rev. Lett. **68**, 1803 (1992).
[62] M. Dine, R. G. Leigh, P. Y. Huet, A. D. Linde, and D. A. Linde, Towards the theory of the electroweak phase transition, Phys. Rev. D **46**, 550 (1992).
[63] S. Y. Khlebnikov, Fluctuation—dissipation formula for bubble wall velocity, Phys. Rev. D **46**, R3223 (1992).
[64] P. B. Arnold, One loop fluctuation—dissipation formula for bubble wall velocity, Phys. Rev. D **48**, 1539 (1993).
[65] G. D. Moore and T. Prokopec, Bubble Wall Velocity in a First Order Electroweak Phase Transition, Phys. Rev. Lett. **75**, 777 (1995).
[66] G. D. Moore and T. Prokopec, How fast can the wall move? A study of the electroweak phase transition dynamics, Phys. Rev. D **52**, 7182 (1995).
[67] G. D. Moore and N. Turok, Classical field dynamics of the electroweak phase transition, Phys. Rev. D **55**, 6538 (1997).
[68] P. John and M. G. Schmidt, Do stops slow down electroweak bubble walls?, Nucl. Phys. **B598**, 291 (2001).
[69] A. Megevand and A. D. Sanchez, Velocity of electroweak bubble walls, Nucl. Phys. **B825**, 151 (2010).
[70] S. J. Huber and M. Sopena, The bubble wall velocity in the minimal supersymmetric light stop scenario, Phys. Rev. D **85**, 103507 (2012).
[71] A. Mégevand, Friction forces on phase transition fronts, J. Cosmol. Astropart. Phys. 07 (**2013**) 045.
[72] T. Konstandin, G. Nardini, and I. Rues, From Boltzmann equations to steady wall velocities, J. Cosmol. Astropart. Phys. 09 (2014) 028.
[73] J. Kozaczuk, Bubble expansion and the viability of singlet-driven electroweak baryogenesis, J. High Energy Phys. 10 (2015) 135.
[74] X. Wang, F. P. Huang, and X. Zhang, Bubble wall velocity beyond leading-log approximation in electroweak phase transition, arXiv:2011.12903.
[75] B. Laurent and J. M. Cline, Fluid equations for fast-moving electroweak bubble walls, Phys. Rev. D **102**, 063516 (2020).

[76] M. Gyulassy, K. Kajantie, H. Kurki-Suonio, and L. D. McLerran, Deflagrations and detonations as a mechanism of hadron bubble growth in supercooled quark gluon plasma, Nucl. Phys. **B237**, 477 (1984).
[77] H. Kurki-Suonio, Deflagration bubbles in the quark-hadron phase transition, Nucl. Phys. **B255**, 231 (1985).
[78] K. Kajantie and H. Kurki-Suonio, Bubble growth and droplet decay in the quark hadron phase transition in the early universe, Phys. Rev. D **34**, 1719 (1986).
[79] K. Enqvist, J. Ignatius, K. Kajantie, and K. Rummukainen, Nucleation and bubble growth in a first order cosmological electroweak phase transition, Phys. Rev. D **45**, 3415 (1992).
[80] J. Ignatius, K. Kajantie, H. Kurki-Suonio, and M. Laine, The growth of bubbles in cosmological phase transitions, Phys. Rev. D **49**, 3854 (1994).
[81] H. Kurki-Suonio and M. Laine, Supersonic deflagrations in cosmological phase transitions, Phys. Rev. D **51**, 5431 (1995).
[82] H. Kurki-Suonio and M. Laine, On bubble growth and droplet decay in cosmological phase transitions, Phys. Rev. D **54**, 7163 (1996).
[83] A. Megevand and A. D. Sanchez, Detonations and deflagrations in cosmological phase transitions, Nucl. Phys. **B820**, 47 (2009).
[84] J. R. Espinosa, T. Konstandin, J. M. No, and G. Servant, Energy budget of cosmological first-order phase transitions, J. Cosmol. Astropart. Phys. 06 (2010) 028.
[85] T. Konstandin and J. M. No, Hydrodynamic obstruction to bubble expansion, J. Cosmol. Astropart. Phys. 02 (2011) 008.
[86] L. Leitao and A. Megevand, Hydrodynamics of ultra-relativistic bubble walls, Nucl. Phys. **B905**, 45 (2016).
[87] D. Bodeker and G. D. Moore, Can electroweak bubble walls run away?, J. Cosmol. Astropart. Phys. 05 (2009) 009.
[88] D. Bodeker and G. D. Moore, Electroweak bubble wall speed limit, J. Cosmol. Astropart. Phys. 05 (2017) 025.
[89] A. Azatov and M. Vanvlasselaer, Bubble wall velocity: Heavy physics effects, J. Cosmol. Astropart. Phys. 01 (2021) 058.
[90] A. Megevand and S. Ramirez, Bubble nucleation and growth in very strong cosmological phase transitions, Nucl. Phys. **B919**, 74 (2017).
[91] J. Ellis, M. Lewicki, and J. M. No, On the maximal strength of a first-order electroweak phase transition and its gravitational wave signal, J. Cosmol. Astropart. Phys. 04 (2019) 003.
[92] J. Ellis, M. Lewicki, J. M. No, and V. Vaskonen, Gravitational wave energy budget in strongly supercooled phase transitions, J. Cosmol. Astropart. Phys. 06 (2019) 024.
[93] C. Caprini *et al.*, Detecting gravitational waves from cosmological phase transitions with LISA: An update, J. Cosmol. Astropart. Phys. 03 (**2020**) 024.
[94] M. Breitbach, J. Kopp, E. Madge, T. Opferkuch, and P. Schwaller, Dark, cold, and noisy: Constraining secluded hidden sectors with gravitational waves, J. Cosmol. Astropart. Phys. 07 (2019) 007.
[95] X. Wang, F. P. Huang, and X. Zhang, Phase transition dynamics and gravitational wave spectra of strong first-order phase transition in supercooled universe, J. Cosmol. Astropart. Phys. 05 (**2020**) 045.
[96] A. Megevand and A. D. Sanchez, Supercooling and phase coexistence in cosmological phase transitions, Phys. Rev. D **77**, 063519 (2008).
[97] A. Kosowsky, M. S. Turner, and R. Watkins, Gravitational radiation from colliding vacuum bubbles, Phys. Rev. D **45**, 4514 (1992).
[98] M. Kamionkowski, A. Kosowsky, and M. S. Turner, Gravitational radiation from first order phase transitions, Phys. Rev. D **49**, 2837 (1994).
[99] A. D. Dolgov, D. Grasso, and A. Nicolis, Relic backgrounds of gravitational waves from cosmic turbulence, Phys. Rev. D **66**, 103505 (2002).
[100] A. Kosowsky, A. Mack, and T. Kahniashvili, Gravitational radiation from cosmological turbulence, Phys. Rev. D **66**, 024030 (2002).
[101] G. Gogoberidze, T. Kahniashvili, and A. Kosowsky, The spectrum of gravitational radiation from primordial turbulence, Phys. Rev. D **76**, 083002 (2007).
[102] C. Caprini, R. Durrer, and G. Servant, The stochastic gravitational wave background from turbulence and magnetic fields generated by a first-order phase transition, J. Cosmol. Astropart. Phys. 12 (**2009**) 024.
[103] T. Kahniashvili, L. Kisslinger, and T. Stevens, Gravitational radiation generated by magnetic fields in cosmological phase transitions, Phys. Rev. D **81**, 023004 (2010).
[104] L. Kisslinger and T. Kahniashvili, Polarized gravitational waves from cosmological phase transitions, Phys. Rev. D **92**, 043006 (2015).
[105] P. Niksa, M. Schlederer, and G. Sigl, Gravitational waves produced by compressible MHD turbulence from cosmological phase transitions, Classical Quantum Gravity **35**, 144001 (2018).
[106] A. Roper Pol, S. Mandal, A. Brandenburg, T. Kahniashvili, and A. Kosowsky, Numerical simulations of gravitational waves from early-universe turbulence, Phys. Rev. D **102**, 083512 (2020).
[107] M. Hindmarsh, S. J. Huber, K. Rummukainen, and D. J. Weir, Gravitational Waves from the Sound of a First Order Phase Transition, Phys. Rev. Lett. **112**, 041301 (2014).
[108] J. T. Giblin and J. B. Mertens, Gravitional radiation from first-order phase transitions in the presence of a fluid, Phys. Rev. D **90**, 023532 (2014).
[109] M. Hindmarsh, S. J. Huber, K. Rummukainen, and D. J. Weir, Numerical simulations of acoustically generated gravitational waves at a first order phase transition, Phys. Rev. D **92**, 123009 (2015).
[110] M. Hindmarsh, S. J. Huber, K. Rummukainen, and D. J. Weir, Shape of the acoustic gravitational wave power spectrum from a first order phase transition, Phys. Rev. D **96**, 103520 (2017).
[111] M. Hindmarsh, Sound Shell Model for Acoustic Gravitational Wave Production at a First-Order Phase Transition in the Early Universe, Phys. Rev. Lett. **120**, 071301 (2018).
[112] M. Hindmarsh and M. Hijazi, Gravitational waves from first order cosmological phase transitions in the sound shell model, J. Cosmol. Astropart. Phys. 12 (2019) 062.

[113] H.-K. Guo, K. Sinha, D. Vagie, and G. White, Phase transitions in an expanding universe: Stochastic gravitational waves in standard and non-standard histories, J. Cosmol. Astropart. Phys. 01 (**2021**) 001.
[114] C. Caprini *et al.*, Science with the space-based interferometer eLISA. II: Gravitational waves from cosmological phase transitions, J. Cosmol. Astropart. Phys. 04 (2016) 001.
[115] L. Leitao and A. Megevand, Spherical and non-spherical bubbles in cosmological phase transitions, Nucl. Phys. **B844**, 450 (2011).
[116] A. Kosowsky and M. S. Turner, Gravitational radiation from colliding vacuum bubbles: Envelope approximation to many bubble collisions, Phys. Rev. D **47**, 4372 (1993).
[117] S. J. Huber and T. Konstandin, Gravitational wave production by collisions: More bubbles, J. Cosmol. Astropart. Phys. 09 (2008) 022.
[118] D. J. Weir, Revisiting the envelope approximation: Gravitational waves from bubble collisions, Phys. Rev. D **93**, 124037 (2016).
[119] H. L. Child and J. T. Giblin, Jr., Gravitational radiation from first-order phase transitions, J. Cosmol. Astropart. Phys. 10 (2012) 001.
[120] D. Cutting, M. Hindmarsh, and D. J. Weir, Gravitational waves from vacuum first-order phase transitions: From the envelope to the lattice, Phys. Rev. D **97**, 123513 (2018).
[121] D. Cutting, E. G. Escartin, M. Hindmarsh, and D. J. Weir, Gravitational waves from vacuum first order phase transitions II: From thin to thick walls, Phys. Rev. D **103**, 023531 (2021).
[122] R. Jinno and M. Takimoto, Gravitational waves from bubble collisions: An analytic derivation, Phys. Rev. D **95**, 024009 (2017).
[123] R. Jinno and M. Takimoto, Gravitational waves from bubble dynamics: Beyond the envelope, J. Cosmol. Astropart. Phys. 01 (2019) 060.
[124] T. Konstandin, Gravitational radiation from a bulk flow model, J. Cosmol. Astropart. Phys. 03 (2018) 047.
[125] A. Megevand and F. A. Membiela, Gravitational waves from bubble walls, J. Cosmol. Astropart. Phys. 10 (2021) 073.
[126] R. Jinno, S. Lee, H. Seong, and M. Takimoto, Gravitational waves from first-order phase transitions: Towards model separation by bubble nucleation rate, J. Cosmol. Astropart. Phys. 11 (2017) 050.
[127] A. H. Guth and S. Tye, Phase Transitions and Magnetic Monopole Production in the Very Early Universe, Phys. Rev. Lett. **44**, 631 (1980).
[128] A. H. Guth and E. J. Weinberg, Cosmological consequences of a first order phase transition in the SU(5) grand unified model, Phys. Rev. D **23**, 876 (1981).
[129] M. S. Turner, E. J. Weinberg, and L. M. Widrow, Bubble nucleation in first order inflation and other cosmological phase transitions, Phys. Rev. D **46**, 2384 (1992).
[130] S. R. Coleman, The fate of the false vacuum. 1. Semiclassical theory, Phys. Rev. D **15**, 2929 (1977).
[131] C. J. Callan and S. R. Coleman, The fate of the false vacuum. 2. First quantum corrections, Phys. Rev. D **16**, 1762 (1977).
[132] A. D. Linde, Fate of the false vacuum at finite temperature: Theory and applications, Phys. Lett. **100B**, 37 (1981).
[133] A. D. Linde, Decay of the false vacuum at finite temperature, Nucl. Phys. **B216**, 421 (1983).
[134] A. Mégevand and S. Ramírez, Bubble nucleation and growth in slow cosmological phase transitions, Nucl. Phys. **B928**, 38 (2018).
[135] A. Mégevand and F. A. Membiela, Bubble wall correlations in cosmological phase transitions, Phys. Rev. D **102**, 103514 (2020).
[136] D. Croon, O. Gould, P. Schicho, T. V. I. Tenkanen, and G. White, Theoretical uncertainties for cosmological first-order phase transitions, J. High Energy Phys. 04 (2021) 055.
[137] H.-K. Guo, K. Sinha, D. Vagie, and G. White, The benefits of diligence: How precise are predicted gravitational wave spectra in models with phase transitions?, J. High Energy Phys. 06 (2021) 164.
[138] L. Leitao and A. Megevand, Hydrodynamics of phase transition fronts and the speed of sound in the plasma, Nucl. Phys. **B891**, 159 (2015).
[139] J. Ellis, M. Lewicki, and V. Vaskonen, Updated predictions for gravitational waves produced in a strongly supercooled phase transition, J. Cosmol. Astropart. Phys. 11 (2020) 020.
[140] F. Giese, T. Konstandin, and J. van de Vis, Model-independent energy budget of cosmological first-order phase transitions—A sound argument to go beyond the bag model, J. Cosmol. Astropart. Phys. 07 (2020) 057.
[141] F. Giese, T. Konstandin, K. Schmitz, and J. Van De Vis, Model-independent energy budget for LISA, J. Cosmol. Astropart. Phys. 01 (2021) 072.
[142] C. Caprini, R. Durrer, T. Konstandin, and G. Servant, General properties of the gravitational wave spectrum from phase transitions, Phys. Rev. D **79**, 083519 (2009).
[143] C. Caprini and D. G. Figueroa, Cosmological backgrounds of gravitational waves, Classical Quantum Gravity **35**, 163001 (2018).
[144] C. Caprini and R. Durrer, Gravitational waves from stochastic relativistic sources: Primordial turbulence and magnetic fields, Phys. Rev. D **74**, 063521 (2006).
[145] C. Caprini, R. Durrer, and R. Sturani, On the frequency of gravitational waves, Phys. Rev. D **74**, 127501 (2006).
[146] O. Gould, S. Sukuvaara, and D. Weir, Vacuum bubble collisions: From microphysics to gravitational waves, Phys. Rev. D **104**, 075039 (2021).
[147] M. Lewicki and V. Vaskonen, Gravitational wave spectra from strongly supercooled phase transitions, Eur. Phys. J. C **80**, 1003 (2020).
[148] M. Lewicki and V. Vaskonen, Gravitational waves from colliding vacuum bubbles in gauge theories, Eur. Phys. J. C **81**, 437 (2021).